Energy Division
Research Institute on Nuclear Systems for a Low Carbon Energy Production
Department of Nuclear Technology

Experimental and Numerical Analysis of a Transverse Shock Wave Propagation Through a Flexible Tube Bundle using the SIMLab Shock Tube Facility

Vincent FAUCHER[1], Vegard AUNE[3,4], Samy MOKHTARI[1,2]

Reference DES/IRESNE/DTN/Dir/2020-05-INDEX-A

1. French Energy Commission (CEA), DES/IRESNE/DTN, Site of Cadarache, F-13108 Saint-Paul-Lez-Durance, France
2. MAST-EMGCU, Université Gustave Eiffel, IFSTTAR, FR-77454 Marne-la-Vallée, France
3. Structural Impact Laboratory (SIMLab), Department of Structural Engineering, Norwegian University of Science and Technology (NTNU), NO-7491 Trondheim, Norway
4. Centre for Advanced Structural Analysis (CASA), NTNU, NO-7491 Trondheim, Norway

Document issued in the framework of the agreement CEA-FRAMATOME-EDF
Tripartite Institute 2020 - F35158

IRESNE

Research institute for nuclear systems for a low carbon energy production

Atomic Energy and Alternative Energies Commission
Center of Cadarache | Building 710 – 13108 Saint Paul lez Durance
T+33 (0)4 42 25 20 01 | nadine.labbal@cea.fr
State-owned industrial and commercial establishment | RCS Paris B 775 685 019

Energy Division
Department of Nuclear Technology

Document property of CEA, issued in the framework of the agreement Tripartite Institute 2020 - F35158
Reproduction and transmission governed by the terms of the agreement

LEVEL OF CONFIDENTIALITY				
DO	DR	CCEA	CD	SD
X				

PARTNERS/CLIENTS	AGREEMENT	TYPE OF ACTION
EDF-FRAMATOME	CEA-FRAMATOME-EDF Tripartite Institute 2020-F35158	80-10-10

CEA INTERNAL REFERENCES			
PROGRAM DIRECTION	DOMAIN	PROJECT	EOTP
DPE	Gen 2 & 3	FUEL ASSEMBLY	A-ASSEM-03-07
MILESTONE	MILESTONE NAME	CONTRACTUAL CONFIDENTIALITY PERIOD	LABORATORY NOTEBOOK
N/A	N/A	N/A	N/A

VERSION TRACKING			
INDEX	DATE	EVOLUTION CONTENT	PAGES,CHAPTERS
A	2020/06/14	Initial issue	60,5

	NAME	POSITION	SIGNATURE	DATE
AUTHORS	V. FAUCHER	Project Manager CEA	Signature numérique de FAUCHER Vincent VF214404B Date : 2020.06.15 06:55:47 +02'00'	2020/06/15
	V. AUNE	Associate Professor NTNU	Vegard Aune	2020/06/15
AUDITOR	G. RICCIARDI	Senior Researcher	RICCIARDI Guillaume 211416	Signature numérique de RICCIARDI Guillaume 211416 Date : 2020.06.15 09:10:14 +02'00'
APPROVER	J. PEYBERNES	Head of Laboratory	PEYBERNES Jean 133057	Signature numérique de PEYBERNES Jean 133057 Date : 2020.06.15 09:53:07 +02'00'
ISSUER	D. ROCHWERGER	Head of Department	ROCHWERGER Daniel DR202273B	Signature numérique de ROCHWERGER Daniel DR202273B Date : 2020.06.15 20:28:23 +02'00'

Document property of CEA, issued in the framework of the agreement Tripartite Institute 2020 - F35158
Reproduction and transmission governed by the terms of the agreement

KEYWORDS

SIMLab Shock Tube facility ; tube bundle dynamics under shock loading ; 3D detailed simulations with EUROPLEXUS software

SUMMARY / CONCLUSIONS

A first series of tests has been successfully performed in the SIMLab Shock Tube facility to provide some insights regarding the dynamic response of a tube bundle submitted to a shock wave. The tests have provided very valuable results in terms of both pressure in the tube and resulting structural kinematics. The experiment has been extensively analyzed using numerical solutions to extend the measures and perform interesting steps towards the validated usage of 3D detailed Fluid-Structure simulations to produce reference solutions to build upper scale of the bundle coupled dynamics, which is the main research topic of Samy Mokhtari's PhD motivating this work.
Some limitations have inevitably been encountered in this beginning research and the experimental results cannot be used directly to provide information about the transfer function associated to the bundle regarding the pressure signals upstream and downstream the specimen. This is mainly due to the large bypasses on both sides of the bundle, finally preventing the incoming wave to actually cross the bundle as it can be expected in the reference PWR configuration. Numerical simulations can also be further improved by taking into account the actual membrane opening dynamics for a better reproduction of the incoming pressure signals, as well as testing the sensitivity of the solution to modelling parameters in the vicinity of the bundle and its supporting box (*i.e.* the boundary conditions at the extremities of the rods and the potential fluid flow between the lateral walls of the box and those of the shock tube). This opens some interesting leads to continue and strengthen the collaboration between NTNU and CEA to keep producing knowledge on this subject of great value for nuclear safety.
Note: CEA thanks NTNU and SIMLab for making it possible to run those tests in their shock tube facility. This was a great opportunity for collective work and knowledge production, decided on quite a short notice and which would have been impossible without the curiosity, the enthusiasm and the sense of welcome of the local team in Trondheim.

DISTRIBUTION (BY EMAIL):

Framatome (Lyon)	Hubert SALAÜN, Guy GENTET, Julien PACULL, Nicolas LAMORTE, Benjamin FARGES, Jean-François DESSEIGNES, Pascal DESCOT, Benoit BARBIER
EDF/R&D	Fabien GRANGE, Adriana MATTIELLO, Pierre MOUSSOU, Pierre BADEL
EDF/DCN	Anne-Francoise COTTE, Julie ADJIMAN
EDF/Direction Technique	Jean-Jérôme VERMOYAL, Isabelle POLI, Steeve EKOMIE-ENGONE, Benoît GURRET, Elodie RICOU
NTNU/SIMLab/SFI CASA	Vegard AUNE, Tore BØRVIK, Magnus LANGSETH
Université Gustave Eiffel, IFSTTAR	Pierre ARGOUL, Lucas ADELAIDE
CEA/DES/DPE	Patrick DUMAZ, Thierry FORGERON
CEA/DES/DGCP	Annie SONIAK
CEA/DES/IRESNE/DTN/Dir	Daniel ROCHWERGER, Caroline TRUFFIER, Vincent FAUCHER
CEA/DES/IRESNE/DTN/STCP/Dir	Olivier GASTALDI, Richard MAZOYER
CEA/DES/IRESNE/DTN/STCP/LETH	Eric VERLOO, Eric BOCCACCIO, Philippe LATIL, Laurent MARCQ
CEA/DES/IRESNE/DTN/STCP/LTHC	Jean PEYBERNES, Lionel ROSSI, Guillaume RICCIARDI, Fabrice FRANCOIS, Samy MOKHTARI
CEA/DES/ISAS/DM2S/Dir	Thomas LAPORTE
CEA/DES/ISAS/DM2S/SEMT/Dir	Valérie VANDENBERGHE, Yann KAYSER
CEA/DES/ISAS/DM2S/SEMT/DYN	Claire GAUTHIER, Pascal GALON, Olivier JAMOND, Nicolas LELONG, Xavier DELAUNE

Document property of CEA, issued in the framework of the agreement Tripartite Institute 2020 - F35158
Reproduction and transmission governed by the terms of the agreement

Contents

Document property of CEA, issued in the framework of the agreement Tripartite Institute 2020 - F35158
Reproduction and transmission governed by the terms of the agreement

1 Introduction

1.1 General framework

This work is part of preliminary research intended to understand, and then model, the dynamic response of a Pressurized Water Reactor fuel assembly to a transverse pressure wave. A PWR operates a high pressure and high temperature, namely 155 bars and 310°C respectively, and such a wave propagation can occur in the event of a sudden opening within the primary loop of the reactor (see Figure 1, extracted from Ref. [1] with courtesy, for an illustration). This accidental scenario is known as Loss of Coolant Accident and the demonstration has to be made that the main reactor core, composed of all fuel assemblies inside the primary vessel (see again Figure 1), can still be properly cooled after the mechanical transient originating from the interaction of the rarefaction wave coming from the pipe break and the internal core structures. This particularly means that the final shape of the fuel assemblies must be compatible with the operation of the nuclear reaction controlling mechanisms. Obviously, such a safety demonstration is already available for the French nuclear power plants, but it inevitably involves penalizing margins to account for some unknown phenomena, concerning for instance the core transient dynamics among many others. The proposed work thus aims at contributing to the reduction of those margins by improving the knowledge and prediction of the core final state in response to a given pipe opening scenario.

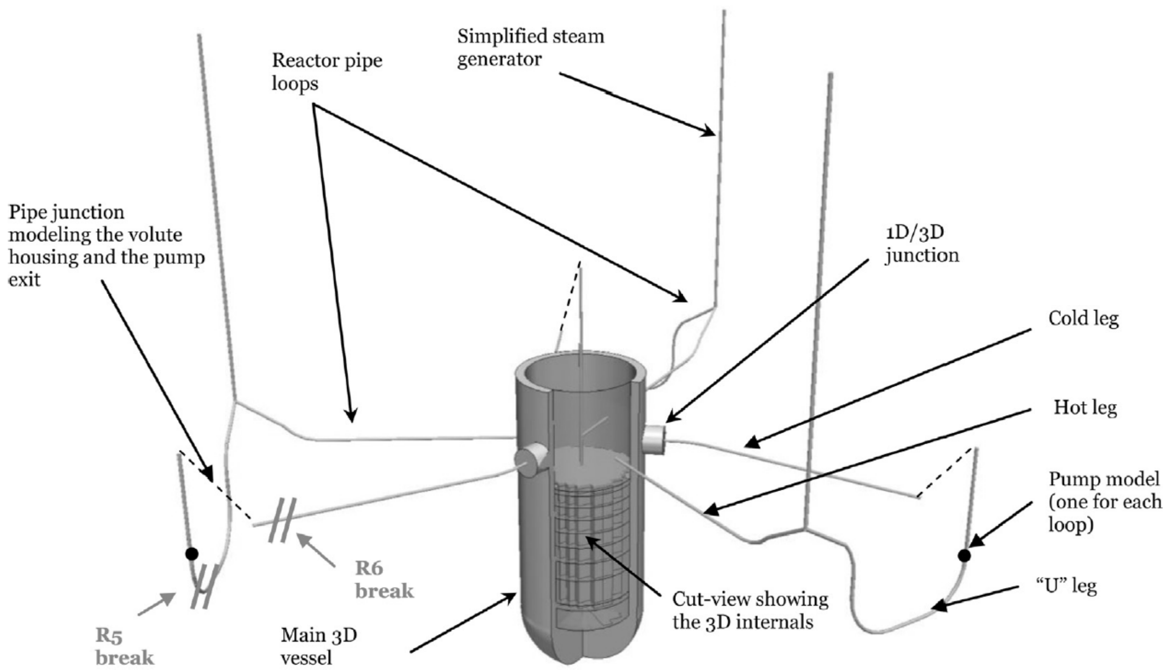

Figure 1: Simplified 1D/3D scheme of a PWR in a LOCA context - reproduced from Ref. [1] with permission

More precisely, given the particular geometry of PWR fuel assemblies illustrated in Figure 2, the interaction between a pressure wave and such a structure is very different whether the transverse and longitudinal component of the wave is concerned. The longitudinal problem can be addressed through a combination of well-chosen head-loss coefficients, to account for the friction along the bundle sections and inside the grids, and additional acoustics impedances, to account for the dynamic effects on the grids on the wave propagations. Such models can be applied seeing each fuel assembly as an equivalent beam and thus can easily be extended at the full core level. On the contrary, the transverse problem is more dependent from the actual interaction between the propagating wave and the fuel assembly microstructure, especially in the bundle sections that contribute the most to the interaction. This latter topic is addressed by the work presented in this report.

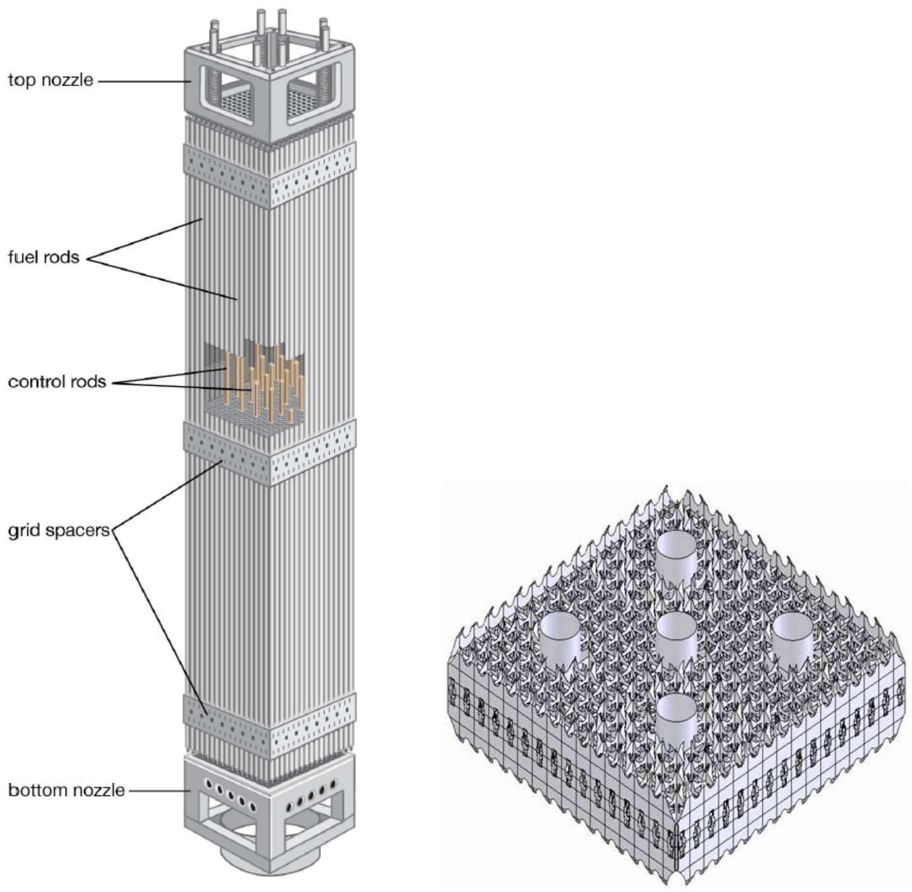

(a) (b)

Figure 2: PWR fuel assemblies generic design: fuel assembly (a) and spacer grid (b).

1.2 Link with Samy Mokhtari's PhD

A PWR core gathers several hundreds of fuel assemblies in the main vessel. Running transient simulations with Fluid-Structure Interaction at local scale is unaffordable to predict its response under pressure wave loading. A description at macroscale, namely the scale of one fuel assembly in the transverse cross section, is thus mandatory. Such a work involves techniques inherited from porous

Document property of CEA, issued in the framework of the agreement Tripartite Institute 2020 - F35158
Reproduction and transmission governed by the terms of the agreement

media and homogenization approaches. Some previous valuable work exists in the case of seismic loading (see for instance Ref. [2]), but the fluid is then considered as incompressible and turbulent, with a particular attention paid to the flow induced damping on the vibratory dynamics of the fuel assembly. In particular, the fluid gradients (density and pressure) are ignored in the cross section of the assembly and the local fluid forces are deduced from variables at macroscale using semi-empiric models accounting for the effect of the turbulent boundary layer on the rods and the grids. Switching from incompressible flow to transient wave propagation, i.e. from Navier-Stokes equations to Euler equations for the fluid, questions the hypotheses made for the seism situation and yields the need for a completely new way of building homogenized fluid variables.

As introduced in the previous subsection, the microstructure of a fuel assembly has only to be considered in a plane cross section within a bundle section, where the pressure gradient are responsible for the forces acting on structures. The pattern of interest for homogenization is thus described in Figure 3. It can be easily extended to 3D with a classical discretization of the fluid variables defined in the cross section along the longitudinal direction in which the assembly can seen as an equivalent beam.

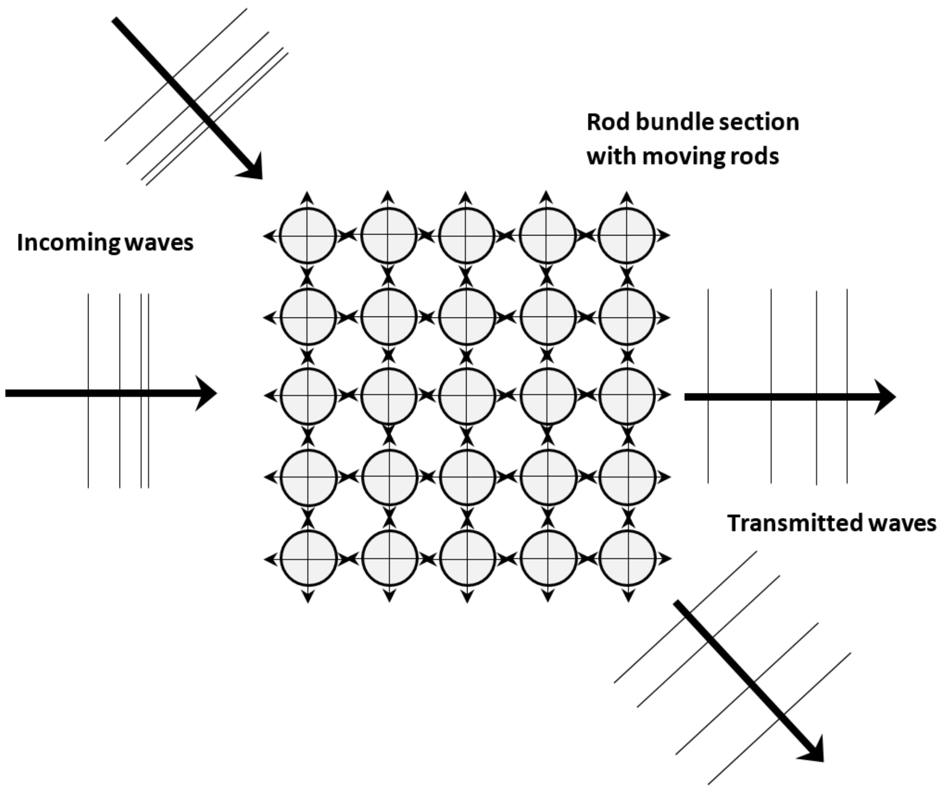

Figure 3: Wave propagation through the cross section of a flexible tube bundle

Defining an accurate and efficient strategy to build relevant fluid variables at the assembly scale and use them to build a filtered and homogenized version of the Euler equations, to be used in interaction

Document property of CEA, issued in the framework of the agreement Tripartite Institute 2020 - F35158
Reproduction and transmission governed by the terms of the agreement

with the structural motion, is the research topic of the PhD of Samy Mokhtari, jointly carried out in France at Gustave Eiffel University under the direction of Pr. Pierre Argoul and technical supervision of Dr. Lucas Adelaïde, and at CEA under the technical supervision of Dr. Guillaume Ricciardi and Dr. Vincent Faucher.

Without entering into details about the ongoing theoretical and modeling work, with some elements available in Ref. [3], reference solutions are needed to assess the capability of the homogenized models in terms of balance between accuracy regarding the preservation of relevant quantities for Fluid-Structure Interaction on the one hand, and computational efficiency on the other hand. Such solutions can be obtained numerically, for instance using EUROPLEXUS software (http://www-epx.cea.fr), dedicated to the local simulations of this kind of transients. An experimental reference is yet mandatory in the process to demonstrate the validity of the local scale numerical solutions and provide the necessary basis to the proposed upscaling strategy.

1.3 Purpose and expectations for the test carried out in SIMLab

The purpose of the collaborative test program initiated between CEA and NTNU is to provide a first set of experimental results to evaluate the capabilities of a homogenized model of a tube bundle under pressure wave loading in its early state. The Simlab shock tube shows very interesting perspectives in this context, since the dimensions of its cross section allows implementing a simplified yet representative tube bundle specimen and it is capable of generating a well-mastered and measured pressure wave loading to produce some significant knowledge and understanding of how the pressure signal is modified when travelling through the bundle.

In an effort to find a satisfactory balance between complexity and representativity, a bundle of 10x10 rods is chosen, with dimensions for rod diameter and spacing between rods close to the regular values for PWR fuel assembly, the preservation of the ratio between the two being a priority constraint. These bundle size and dimensions especially enable the possibility to perform 3D detailed simulations of the test, as well as having a significant part of the device accessible through the windows in the dedicated section of the shock tube.

As far as expectations are concerned, this tests must definitely be considered as part of preliminary towards the industrial goal expressed in preceding sections. The results shall be looked at taking into account the following questions.

- Is it possible to identify experimentally a transfer function associated to the bundle connecting well-chosen variables upstream and downstream the specimen ?
- Are the detailed 3D simulations sufficiently close to the measures (both pressure sensors and fast camera images (see Section 2.1 for some details) to provide be used as extended reference data to confront the homogenized model in construction ?
- What lessons can be learned from this first series of tests to improve the experimental basis to come along with the ongoing research dedicated to fuel assembly modeling in LOCA situation ?

Document property of CEA, issued in the framework of the agreement Tripartite Institute 2020 - F35158
Reproduction and transmission governed by the terms of the agreement

Regarding the test setup in this preliminary experimental step, only the case where the wave front is parallel to one face of the square bundle will be investigated (see Figure 3). Moreover, the experiment will obviously be carried out in air given the shock tube technical conditions. This significantly changes the compressibility of the fluid compared to pressurized water and will have to be discussed in the interpretation of the tests.

To close this introductive section, CEA would like to thank sincerely NTNU and SIMLab for making it possible for us to run those tests in their shock tube facility. This was a great opportunity for collective work and knowledge production, decided on quite a short notice and which would have been impossible without the curiosity, the enthusiasm and the sense of welcome of the local team in Trondheim.

2 Experimental setup

2.1 The SIMLab shock tube facility

The tests were performed in the SIMLab Shock Tube Facility (SSTF) at NTNU. A detailed presentation of the overall shock tube design and an evaluation of its performance can be found in Ref. [4]. The SSTF has proven to be an easily controllable alternative to generate shock waves and can be used to study the dynamic response and fluid-structure interaction (FSI) of shock-loaded structures. The SSTF consists of several parts joined together using bolted connections of 24 M24 socket-head screws at the end flanges of each part (see Figure 4a). Rubber O-rings are recessed into the flange surfaces to ensure sealing at the joints. Each part is equipped with steel wheels and is carried by a two-rail support of L-shaped angle brackets for convenient assembly and disassembly of the tube. This provides flexibility in varying the length of the driven section. If necessary, it is also possible to fully restrain the tube from axial movement by clamping the rear end of the driver section to the floor. The overall length of the tube is 18.355 m and it is made from stainless steel of grade P355NH which is intended for pressure purposes according to the European standard EN 13445 [5].

The driver section (Figure 4a) is manufactured with a total length of 2.02 m and has an inner diameter of 0.331 m where the internal wall is dull polished to obtain a smooth surface. Aluminium inserts may be used to vary the length of the driver section in 0.25 m increments. The driver is followed by a 0.14-m-long firing section which consists of several intermediate pressure chambers separated by diaphragms (Figure 4a and 4c). This enables the total pressure difference between the driver and driven sections to be achieved stepwise. Several ports have been machined on the driver flange and circumference of the firing section to provide connections to pressure sensors, venting, and evacuation lines. The experiment starts by filling the driver and firing sections with compressed air, where the pressures in the intermediate chambers are operated below the diaphragm rupture strength such that the desired pressure p_4 is obtained in the driver. A LabVIEW program has been developed and solenoid valves (ASCO Series 223) are installed on the gas-filling lines to control the filling process, making this operation fully automated based on signals given by the pressure sensors (BAUMER PBMN-24B31) monitoring the driver and intermediate pressure chambers. Rupture of the diaphragms is initiated by controlled and rapid venting of the intermediate pressure closest to the driver section (see Figure 4c), using two solenoid valves (ASCO Series 223). This ensures a controlled rupture of the diaphragms and reproducible bursting pressures. The bursting pressure may be

Document property of CEA, issued in the framework of the agreement Tripartite Institute 2020 - F35158
Reproduction and transmission governed by the terms of the agreement

varied by changing the thickness of the diaphragms. Melinex sheets are used as diaphragms due to its strength and repeatability. It is also possible to use metallic diaphragms if required.

The inner cross-section in the driven section starts with a 0.6-m-long transition region from circular to a square cross-section, where an epoxy material is used to obtain a smooth surface and a square cross-section of 0.3 m $\times$ 0.3 m inside the surrounding tube (Figure 4e). The epoxy material works as a practically incompressible material while the surrounding tube ensures the structural strength. The square cross-section downstream the firing section was chosen to enable the installation of test objects in threaded holes in the tube floor, and to accommodate plane parallel windows (see window section in Figure 4a) which simplifies the use of optical techniques (such as high-speed cameras). The average roughness (Ra) of the surfaces inside the driven section is reported by the manufacturer to be in the range of 0.2 - 0.4 μm.

The driven section ends in a tank of 5.1 m^3 with an internal diameter of 1.6 m (see Figure 4a). This enables mounting of larger test specimens (exposed to localized loading) at the end of the tube, and an increase in volume and overall decrease in pressure after the experiment in open-end configurations.

Piezoelectric pressure sensors (Kistler 603B), corresponding charge amplifiers (Kistler 5064) and data acquisition system from National Instruments (NI USB-6356) are used to measure the pressure downstream the firing section. The mounting of pressure sensors are possible at 20 locations along the driven section by using threaded adapters (Kistler 6501) flush mounted with the internal roof of the tube. A thin layer of insulating silicone (Kistler 1051) is used to shield the pressure sensors against heat transfer from the shock wave since the sensors are only designed for temperatures up to 200 °C.

The maximum working pressure of the driver section is limited to 17 MPa while the driven section, window section and tank are limited to 10, 5 and 1.4 MPa, respectively. All respective parts of the SSTF have been tested at a static pressure 45 % higher than the working pressure for a few minutes to ensure sufficient strength for routine use.

Document property of CEA, issued in the framework of the agreement Tripartite Institute 2020 - F35158
Reproduction and transmission governed by the terms of the agreement

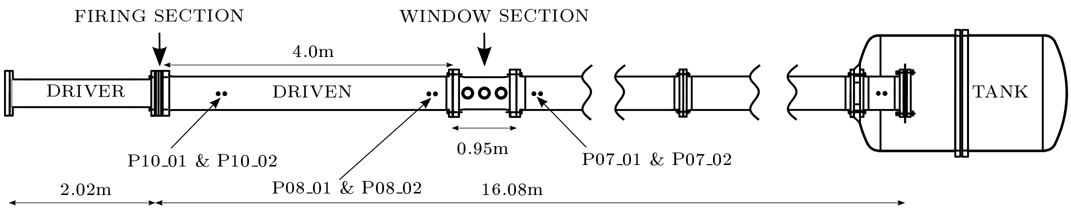

(a)

(b)

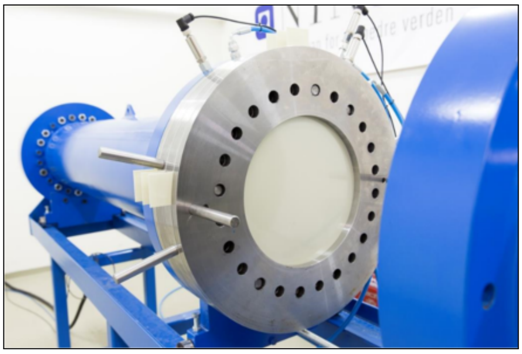

(c)

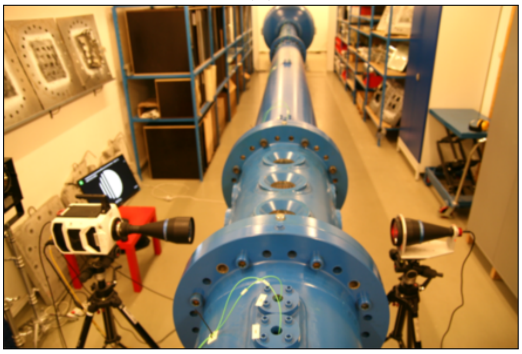

(d)

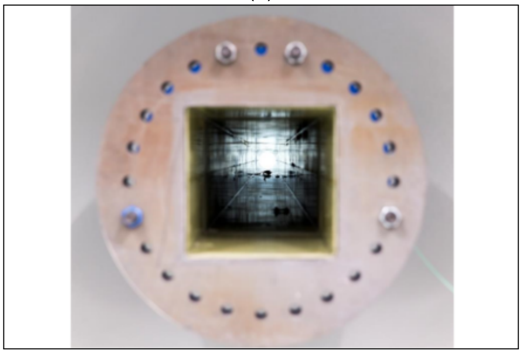

(e)

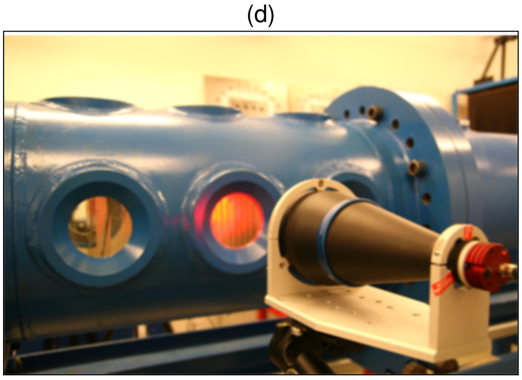

(f)

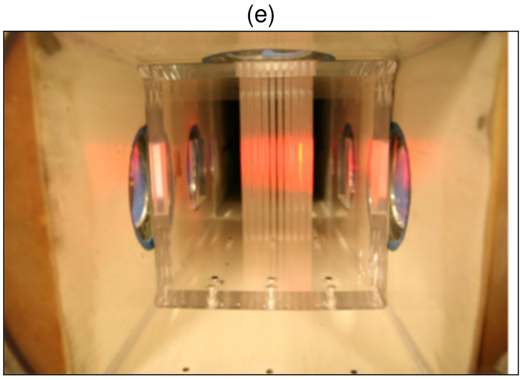

(g)

Figure 4: Experimental setup: (a) Sketches of the SSTF (seen from above), pictures of the (b) entire shock tube facility, (c) firing section, (d) close-up on camera setup, (e) open end and internal cross-section driven section,(f) telecentric lense, and (g) tube bundle. The pictures in (b), (c) and (d) are seen from the driven section, the open end in (e) is seen from the tank, while the tube bundle in (g) is seen from inside the driven section. (b) and (c) are reprints from Ref. [4].

Document property of CEA, issued in the framework of the agreement Tripartite Institute 2020 - F35158
Reproduction and transmission governed by the terms of the agreement

2.2 Specimen design and manufacturing

The specimen has been designed at CEA, France, to place a bundle of 10x10 rods in the main section of the shock tube. The diameter and spacing of the rods are representative of a PWR Fuel Assembly to limit scaling effects regarding the wave propagation through the bundle. Both extremities of the rods are inserted into holes in two horizontal plates. The bottom plate was then to be clamped on the bottom wall of the shock tube using dedicated bolts and tapped holes. The location of the holes in the plate was initially decided to place the first row of rods of the bundle in the middle of the window section of the shock tube. A small misunderstanding in the actual dimensions of the tube, originating apparently in the neglected thickness of the flange connecting the window section to the rest of the tube, resulted in the need to drill another series of holes in the bottom plate just before the test to have the bundle placed in the desired position in the shock tube. This had some unforeseen consequences detailed further in the document. Finally, the top and bottom plates of the specimen and connected together and supported by two lateral plates of the same thickness, in which square windows are cut to allow a direct optical access to the bundle for the telecentric lenses used for the Schlieren representation of the waves in the fluid and for the structural motion imaging. The final section of the supporting structure matches the dimensions of the inner section of the shock tube, with the necessary tolerance (around 1 cm in both transverse directions) to ensure an easy installation in the facility.

A sketch of the specimen and some pictures out of the tube are provided in Figure 5. Bevels are visible on the horizontal and vertical supporting plates (see Subfigures 5a and 5d), in order to limit the perturbation of the incoming wave entering the supporting structure for the bundle. Rows of holes are also visible in the bottom plate (see Subfigures 5b and 5c), for the initial location of the bolts connecting the structure to the shock tube. In particular, there is a row located at the back of the specimen, downstream of the bundle following the wave propagation in the tube, with a key role in taking up the pressure forces applied by the wave on the bundle.

For simplicity within a constrained schedule for the delivery of the specimen, all the components were manufactured with the same material as the rods, *i.e.* polymethyl- methacrylate or PMMA. It was selected for both its flexibility and optical properties, even if the final design implementing windows in the lateral vertical panels makes little use of the latter. One consequence of this choice of material is a brittle behaviour of the supporting structure. This was managed by the disposition of the holes in the initial design of the bottom plate. However, as introduced above, the holes had unfortunately to be shifted of 3 cm towards the back of the specimen to obtain the expected position of the bundle regarding the windows of the visualization section. This mandatory last minute adjustment resulted in the disappearance of the row of bolts located downstream of the bundle and exposed the bottom plate to tensile stress when the pressure wave hit the bundle.

Anyway, the proposed design and manufacturing strategy was successful in providing the test specimen on the right schedule in France, to then be disassembled, transported to Trondheim, Norway, and reassembled and tested during the presence of CEA staff on site.

Document property of CEA, issued in the framework of the agreement Tripartite Institute 2020 - F35158
Reproduction and transmission governed by the terms of the agreement

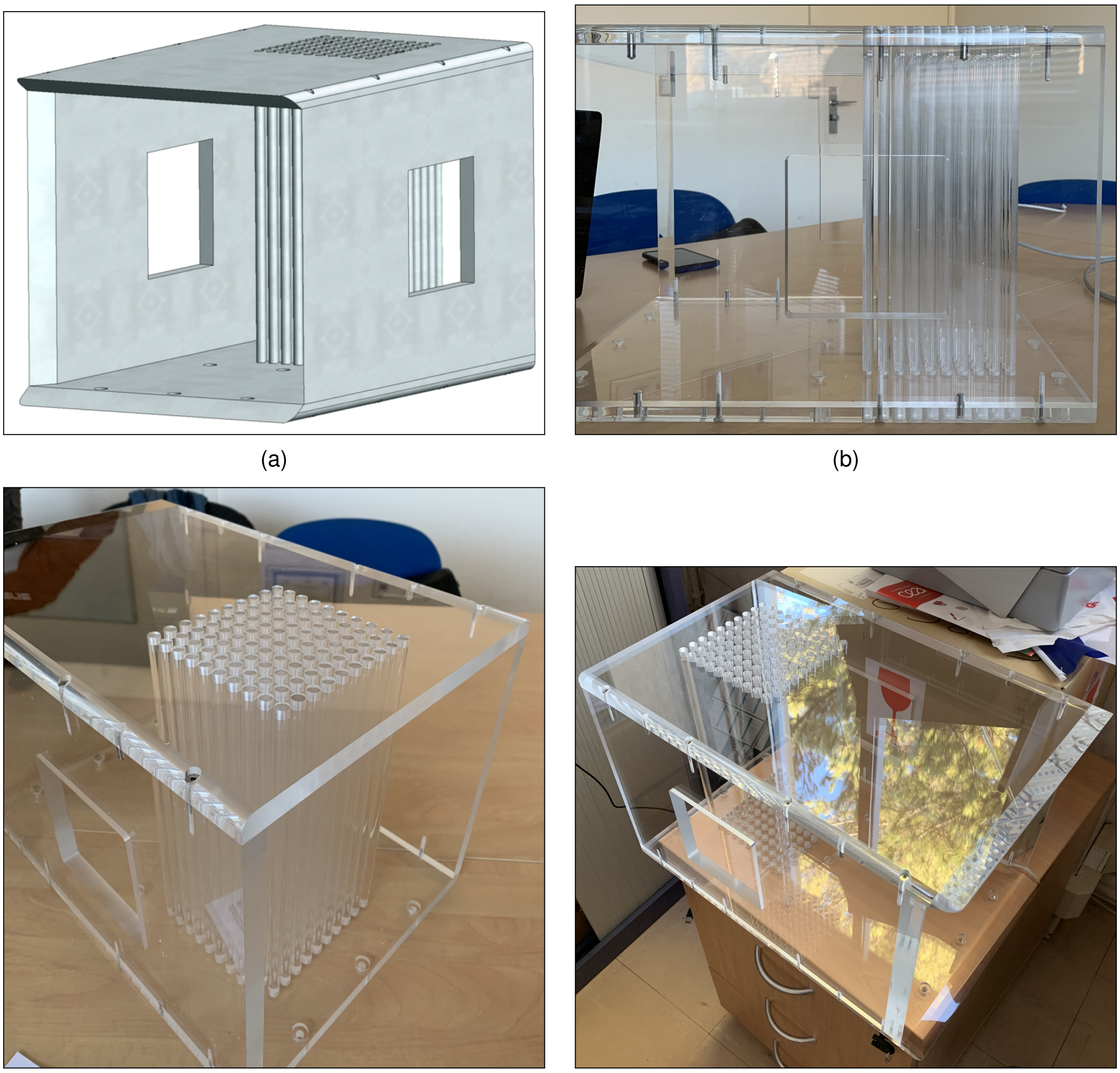

(a) (b) (c) (d)

Figure 5: Sketch and views of the specimen engineered at CEA

3 Experimental results

3.1 Test programme

3.1.1 General conduct of the tests

An illustration of the experimental setups and pictures of the test configurations are shown in Figure 4. The tests operated with a maximum driver length of 2.02 m (Figure 4a). The driven section was operated with a length of 16.08 m, where the first row of tube bundles were located in the center of the window section (see Figures 4f-g). The loading was varied by changing the initial pressure p_4 in the driver section, while the initial pressure in the driven section was operated at ambient conditions (p_1 and T_1). Table 1 gives the complete test matrix, where each test is numbered X-Y in which X denotes open tube without the bundle (O) or tube bundle (B) configuration. Y indicates the firing overpressure (in bars) in the driver. It is worth noting the good repeatability of the bursting characteristics of the diaphragms by comparing the firing pressure p_4 between tests with the same initial conditions in Table 1.

Table 1: Test matrix including initial conditions for each test. Peak pressures p_4 measured in the driver before venting.

Test	Overpressure p_4 in driver (kPa)	Pressure p_1 in driven (kPa)	Temperature (°C)
O02	252.08	99.60	21.67
O05	517.29	98.50	21.19
B02	255.13	100.12	21.15
B05	516.37	100.02	21.40

Pressure measurements from the open-tube (O) tests could then be used as a basis to investigate potential FSI effects in the tests with tube bundle. The main objective is to investigate FSI effects both experimentally and numerically. However, before investigating FSI effects numerically it is necessary to evaluate the performance of the fluid sub-domain in the simulations. This motivated experiments using an open-tube configuration. Open-tube tests may then be used to evaluate the shock wave propagation in the SSTF and the predictive capabilities of the numerical simulations in EPX (see Section 4). Thus, the open-tube tests serve as a quantitative measure for evaluation of purely Eulerian (numerical) simulations and as a reference to study FSI effects of the tube bundle experimentally.

Piezoelectric pressure sensors (Kistler 603B), corresponding charge amplifiers (Kistler 5064) and data acquisition system from National Instruments (NI USB-6356) were used to measure the pressure during the tests. In all tests, six sensors flush mounted in the tube roof measured the pressure behind the incident and reflected shock wave. The location of the sensors are show in Figure 4a, where they are located with an spacing of 10 cm in between each pair (Sensors P07, P08 and P10 are located in pairs). Sensors P10 were located 0.97 m and 1.07 m downstream the diaphragms in the firing section, P08 were located 0.22 m and 0.32 m upstream the window section, while P07 were located 0.22 m and 0.32 m downstream the window section. The delay in arrival time at each pair of sensors may then be used to determine the shock velocity v_s and the corresponding Mach number M_s. The pressure sensors were automatically triggered when the shock wave arrived at the first sensor downstream the firing section and operated with a sampling frequency of 500 kHz. A thin layer of insulating silicone (Kistler 1051) was used to shield the pressure sensors against heat transfer from the shock wave during the tests.

To establish a basis for comparison of the shock wave propagation and the dynamic response of the bundles in the numerical simulations, a high-speed camera with a telecentric setup (OPTO LT-CLHP series) was used for Schlieren photography of the shock wave in both the open-tube (O) and tube bundle (B) tests. The setup of the high-speed camera (Phantom v2511) is illustrated in Figures 4d, 4f and 4g. The high-speed camera was instrumented with a high resolution telecentric lens

Document property of CEA, issued in the framework of the agreement Tripartite Institute 2020 - F35158
Reproduction and transmission governed by the terms of the agreement

(TC4MHR080-F) focusing on a telecentric HP illuminator (LTCLHP080-R) with a beam diameter of 100 mm. Subset digital image correlation (DIC) was used to track the displacement of the first row of bundles in the tube bundle (B) tests, comparing the greyscale-value field of the speckle pattern for an image in the deformed (current) configuration to that at the undeformed (reference) configuration. The sampling rate of the high-speed camera was 37 kHz. The pressure measurements were also synchronized with the high-speed camera, enabling synchronization of pressure signals and high-speed images.

3.1.2 Failure of the supporting structure during the second test

Due the necessary shift of the holes for the bolts connecting the supporting structure to the shock tube mentioned in Section 2.2, the impact of pressure wave on the bundle produced tensile stress in the bottom plate with brittle behaviour. Very small cracks were visible starting from the remaining bolts after the first test (B02). The second test destroyed the specimen, starting with a straight crack near the second row of bolts and continuing with diagonal cracks in the lateral panel, leading to the release of the rear part of the specimen holding the rods in the tube (see Figure 6). It could fortunately be retrieved quite easily with no damage to the facility thanks to the knowledge and expertise of the local team operating the tube.

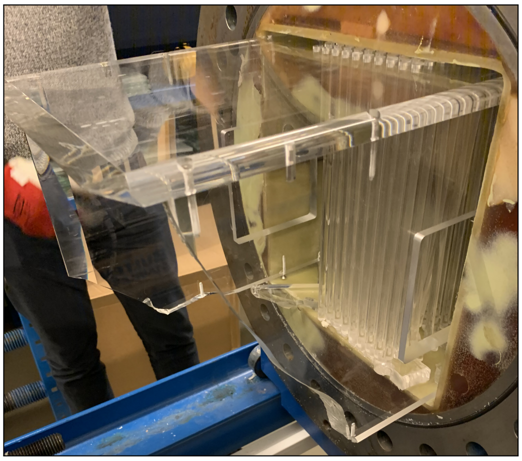

(a) Released part of the specimen retrieved in the tube

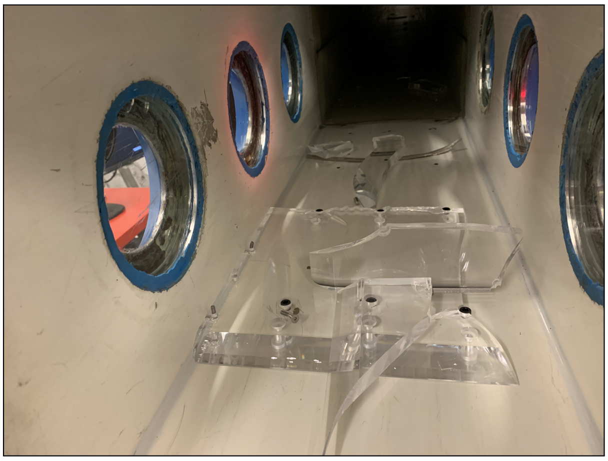

(b) Remaining part of the supporting structure left connected to the tube

Figure 6: Specimen after failure during the second test

Failure occurred after the relevant data was acquired during the second test, making it exploitable. It prevented to test the effect of stronger shocks on the bundle itself, but the displacements measured through the window section for the two successful tests showed that the expected levels were reached with no reservation.

Document property of CEA, issued in the framework of the agreement Tripartite Institute 2020 - F35158
Reproduction and transmission governed by the terms of the agreement

3.2 Firing pressure 2.5 bars

3.2.1 Pressure curves along the tube

The experimental results in terms of pressure curves along the tube from both the O02 test and the B02 test will be presented in the following. Figure 7 contains the pressure histories at the respective sensors in the O02 and B02 tests, while Figure 8 compares the pressure histories at the pressure at the sensors before and after the tube bundle for the O02 and B02 tests. The sensors were flush mounted with the roof of the internal cross-section and positioned 12.275 (P08_01), 12.285 (P08_02), 10.785 (P07_01), 10.885 (P07_02), 15.125 (P10_01) and 15.225 (P10_02) m upstream the open end of the tube (see Figure 4a). The pressure sensors were automatically triggered when the shock wave arrived at P08_01 and operated with a sampling frequency of 500 kHz.

Some preliminary observations:

- Under ideal conditions, the distant flow field is then characterized by the occurrence of a normal shock front of constant strength where the reflected rarefaction waves will eventually decrease the driving pressures. This is observed to some extent at Sensors P10_01 and P10_02, while the pressure histories at the remaining sensors resembles the exponential decay in pressure after the peak pressure. This could be related to both the reflected rarefaction waves and the diaphragm failure process.
- This may indicate that there are some loss of directional energy due to an initial 3D flow in the vicinity of the firing section during the diaphragm opening process. The diaphragm burst starts by tearing at the centre, followed by diagonal tearing and folding back of the petals formed during the opening process. This results in a high velocity jet and 3D flow of the driver gas originating from the expanding hole. The finite opening time causes the shock wave to travel several tube diameters before the wave front is fully formed, and this effect is more evident as the diaphragms become thicker. Thus, increased driver pressures involve more diaphragms of larger thickness resulting in a slower diaphragm opening process preventing satisfactory folding back and increased 3D flow during the opening process.
- Figures 7b and 8a show three distinct jumps in pressure at Sensors P08 for test B02. This implies that there is an influence of both the box and the tube bundle on the pressure recorded upstream the tube bundle. The first jump in pressure is as expected and due to the increase in pressure over the shock wave, while the second and the third jump may be related to reflected pressures due to the box and the tube bundle.

Document property of CEA, issued in the framework of the agreement Tripartite Institute 2020 - F35158
Reproduction and transmission governed by the terms of the agreement

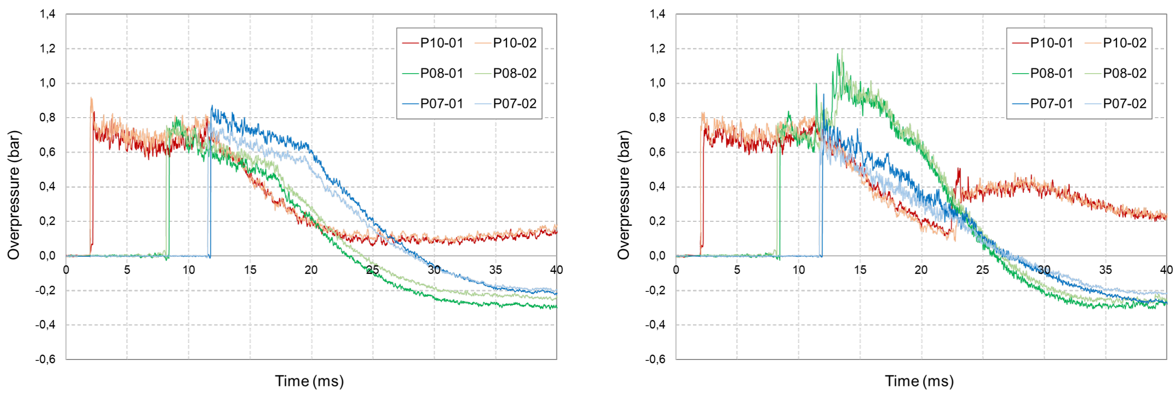

(a) (b)

Figure 7: Pressure measurements along the tube in test: (a) O02 and (b) B02. The number of sensors were limited to 6 channels in the data acquisition system and the respective sensors were positioned 12.275 (P08_01), 12.285 (P08_02), 10.785 (P07_01), 10.885 (P07_02), 15.125 (P10_01) and 15.225 (P10_02) m upstream the open end of the tube (see Figure 4a).

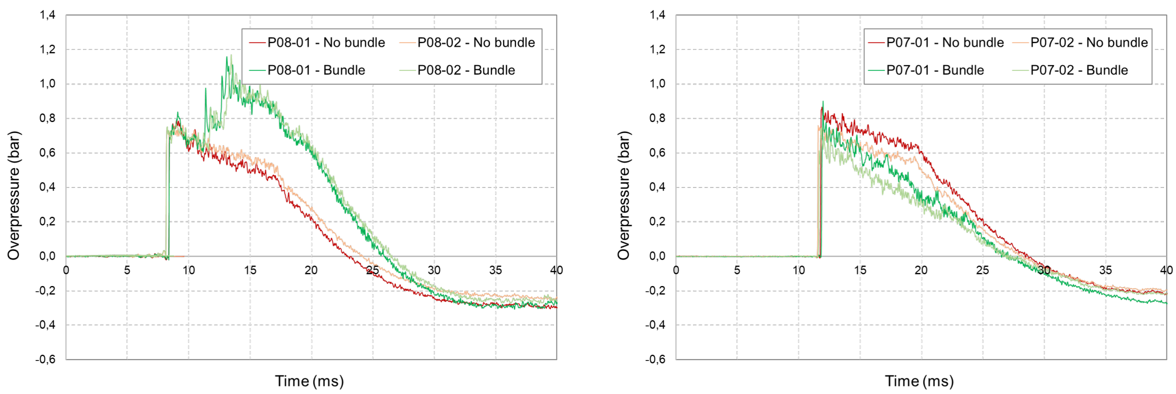

(a) (b)

Figure 8: Pressure measurements in test O02 and B02 at sensors: (a) P08 and (b) P07. The respective sensors were positioned 12.275 (P08_01), 12.285 (P08_02), 10.785 (P07_01) and 10.885 (P07_02) m upstream the open end of the tube (see Figure 4a).

Document property of CEA, issued in the framework of the agreement Tripartite Institute 2020 - F35158
Reproduction and transmission governed by the terms of the agreement

3.2.2 Schlieren vizualization of the rods and the shock wave

The images obtained from the telecentric lenses in terms of a Schlieren-like vizualization will be presented in the following. These measurements provide images of the rods motion and the shock wave propagation close to the tube bundle. The experimental results in this section will be limited to the B02 test, since test O02 was carried out with an open tube without any box or bundle.

Schlieren photography is used to visualize the wave propagation of varying density. This method uses light from a collimated source to focus on an object. Variations in the speed that the light moves through the flow field will then indicate density gradients by distorting the light beam. These distortions results variations in the intensity of the light and are possible to visualize with a high-speed camera. A telecentric illuminator can create such collimated light, and a telecentric lens can be used to collect all the light coming from the illuminator.

Some preliminary observations:

- Figures 9a-9e show the initial, undeformed configuration of the rods prior to the wave impact.
- Figures 16b-9e show an almost planar shock wave on its way to the tube bundle. Similar high-speed images for test O02 show a perfectly planar shock wave. This may indicate that there has been some disturbances of the planar shock wave due to the surrounding box of the tube bundle.
- Figures 9f is more or less the exact point of impact and first interaction between the shock wave and the first row of rods in the tube bundle.
- Figures 9g-9o show that parts of the wave is reflected, parts of the wave interacts with the tube, while the remaining passes on the sides of the tube bundle.
- It also worth noting that the rods have negligible deformations until t = 8.3159 ms (see Figures 9o and 12). This may indicate that the response of the tube bundle is dominated by the drag pressure following the shock wave and not the first interaction with the shock wave itself (shock wave impact).

3.2.3 Displacement bundle

Figure 10 shows a series of images representing the dynamic response of the tube bundle. The dynamic response is obtained using subset digital image correlation (DIC) to track the displacement of the first row of bundles in test B02. Figure 11 attempts to illustrate how this subset DIC is carried out by tracing the greyscale values inside a subset throughout the entire image series (see red square in Figure 11), while Figure 12 shows the corresponding displacement of the first row of bundles in the longitudinal direction of the tube. The subset DIC was carried out using an MATLAB code developed at SIMLab, NTNU.

Some preliminary observations:

- Note that all times of interest (TOI) in Figure 10 are illustrated by black markers in Figure 12.

Document property of CEA, issued in the framework of the agreement Tripartite Institute 2020 - F35158
Reproduction and transmission governed by the terms of the agreement

- Figure 10a shows the point in time when the first row of rods start to move.
- Figure 10b shows the point in time when the first row of rods are half-way to the maximum deformation.
- Figure 10c shows the point in time when the first row of rods reach maximum deflection.
- Figures 10d-10o correspond to the remain times of interest (TOI) in Figure 12.
- Figures 10c-10m indicate that several rods may be in contact to each other during the test.
- Figure 12 shows that that the mid-point of the first row of rods undergoes a rapid deformation from t = 8.4780 ms (Figure 10a) until the point of maximum deflection at t = 10.6672 ms (Figure 10c), before elastic vibrations following a slight linear decreasing trend occurs until t = 22.5320 ms (Figure 10l), then there is observed a distinct drop in magnitude for the dispacement until t = 25.3699 ms (Figure 10m), before the mid-point of the first row of rods seems to undergo elastic vibrations around a slightly permanent deformed configuration throughout the remaining of the test. The mid-point of the first row of rods is indicated by the red marker in Figure 11.
- It is interesting to note the similar shape of the mid-point deflections of the first row of tubes in Figure 12 and the pressure profiles at sensors at P08 in Figure 7. Both starts with a slight linear decaying trend before a small 'kink' followed by an exponential decay.
- Figure 12 indicates a minor plastic deformation (approx. 1.0 mm) of the first row of rods. It should be noted that it is challenging to conclude on the magnitude of plastic deformation in the rods based on the recorded images, since the rods have not fully come to rest at the last image in Figure 10o. There are still some small elastic vibrations around the new permanent configuration of the tubes (see Figure 11).

Document property of CEA, issued in the framework of the agreement Tripartite Institute 2020 - F35158
Reproduction and transmission governed by the terms of the agreement

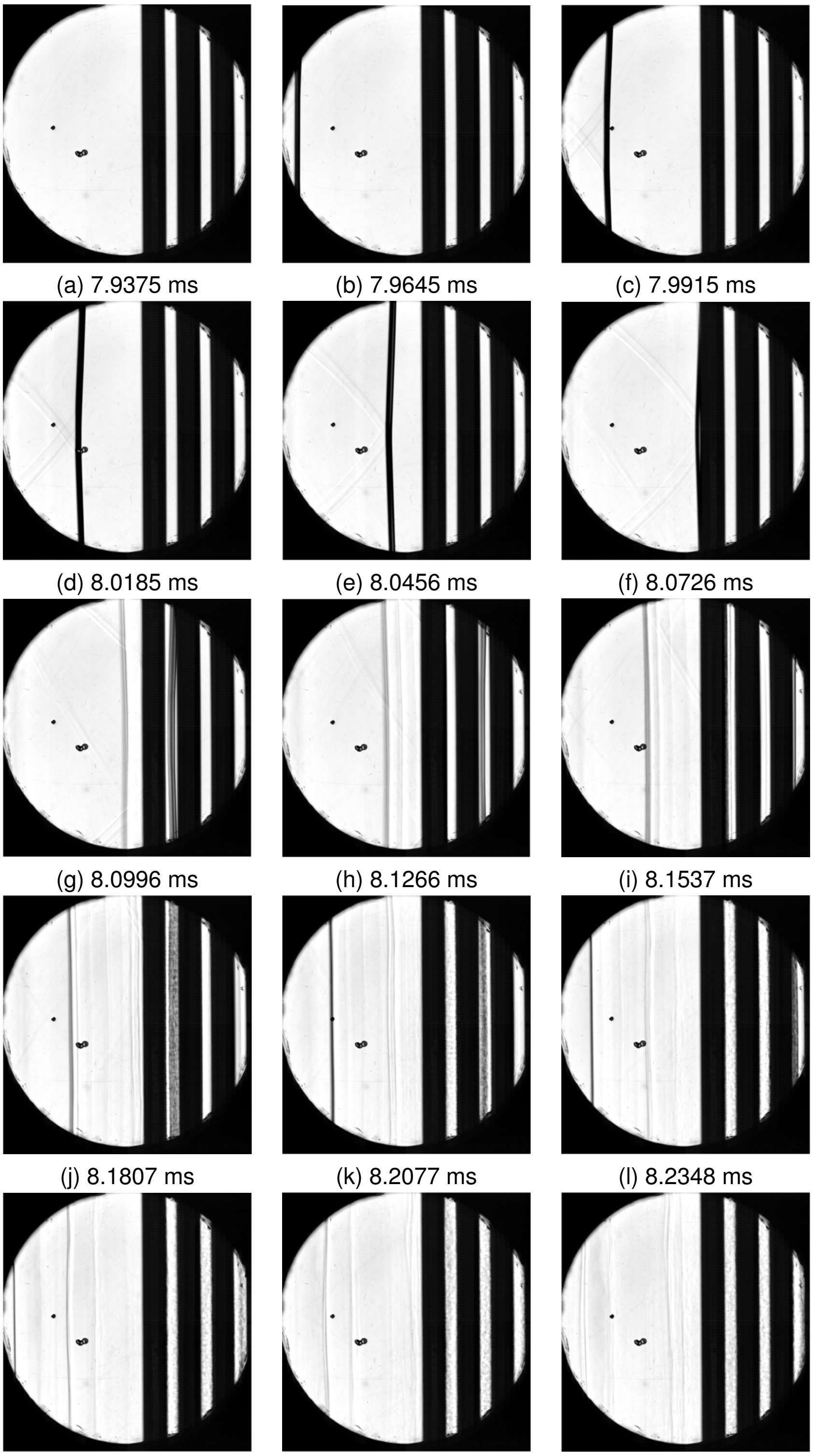

(a) 7.9375 ms (b) 7.9645 ms (c) 7.9915 ms

(d) 8.0185 ms (e) 8.0456 ms (f) 8.0726 ms

(g) 8.0996 ms (h) 8.1266 ms (i) 8.1537 ms

(j) 8.1807 ms (k) 8.2077 ms (l) 8.2348 ms

(m) 8.2618 ms (n) 8.2888 ms (o) 8.3159 ms

Figure 9: Schlieren-like vizualization in test B02 using the telecentric setup in Figures 4d, 4f and 4g. Time zero (t=0) is taken as the arrival of the shock wave at Sensor P10_02.

Document property of CEA, issued in the framework of the agreement Tripartite Institute 2020 - F35158
Reproduction and transmission governed by the terms of the agreement

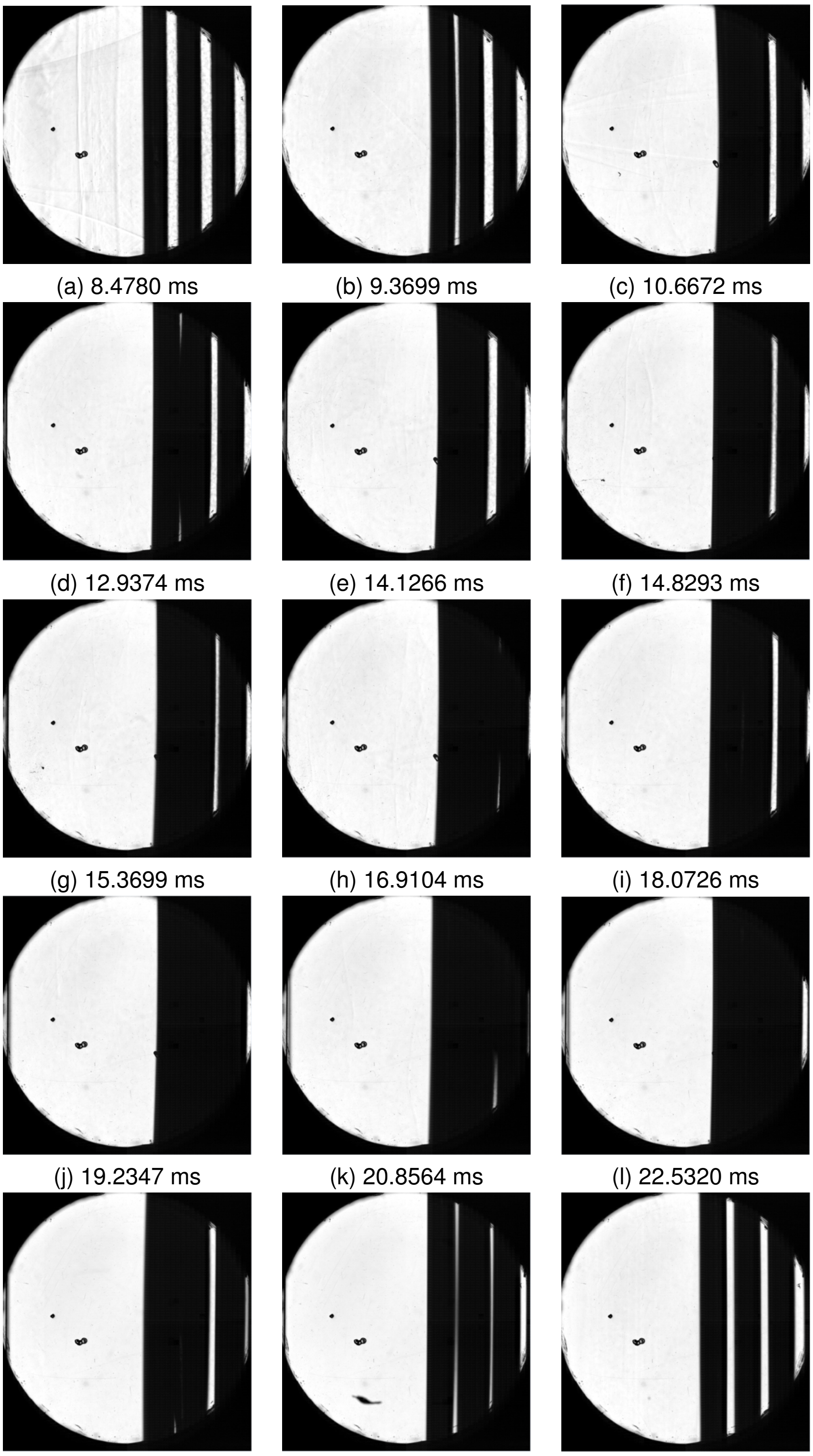

(a) 8.4780 ms (b) 9.3699 ms (c) 10.6672 ms

(d) 12.9374 ms (e) 14.1266 ms (f) 14.8293 ms

(g) 15.3699 ms (h) 16.9104 ms (i) 18.0726 ms

(j) 19.2347 ms (k) 20.8564 ms (l) 22.5320 ms

(m) 25.3699 ms (n) 28.0455 ms (o) 51.5861 ms

Figure 10: Schlieren-like vizualization in test B02 using the telecentric setup in Figures 4d, 4f and 4g. Time zero (t=0) is taken as the arrival of the shock wave at Sensor P10_02.

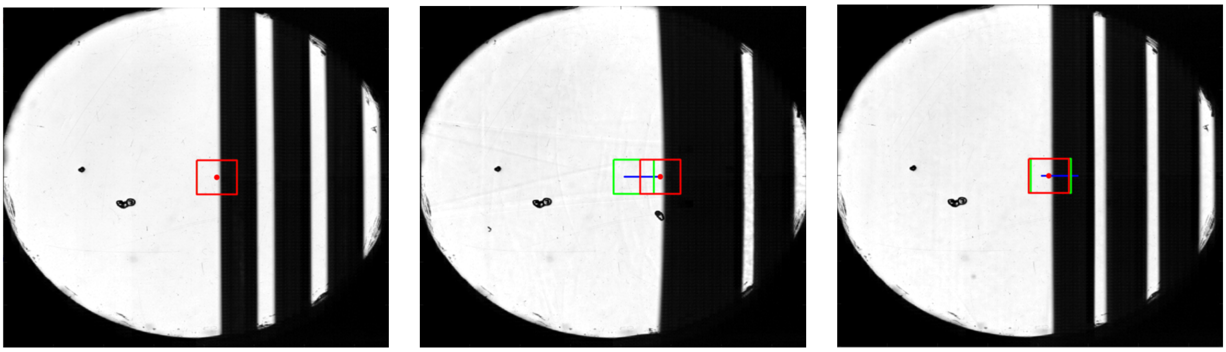

(a) (b) (c)

Figure 11: Illustration of the subset DIC carried out in MATLAB using the images from the using the telecentric setup in Figures 4d, 4f and 4g: (a) first image, (b) image corresponding to the point of maximum deformation in the first row of bundles, and (c) at the last recorded image.

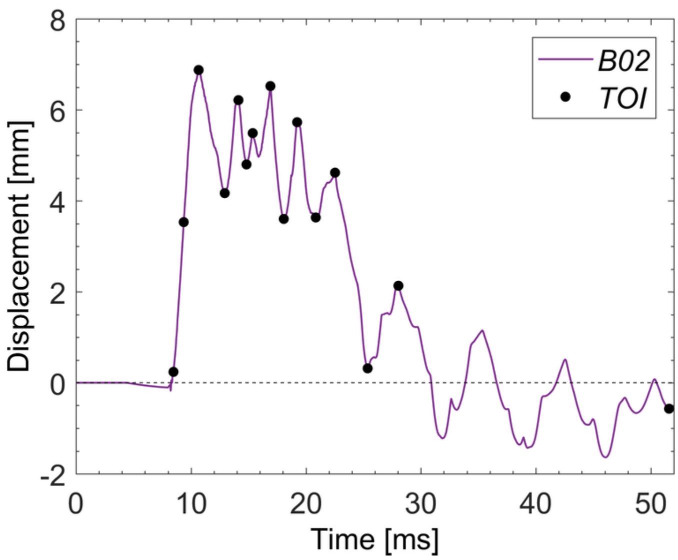

Figure 12: Dynamic response of the first row of bundles in test B02, in terms of displacement in the longitudinal axis of the tube. Time zero (t=0) is taken as the arrival of the shock wave at Sensor P10_02. Black markers corresponds to the times of interest (TOI) in Figure 10.

3.3 Firing pressure 5 bars

Since it was observed only minor permanent deflection on the tube bundle in test B02 (see Figures 10o and 12), it was decided to re-use the box and rods in a new experiment at larger magnitude of pressure. This is referred to as test B05 in Table 1.

3.3.1 Pressure curves along the tube

The experimental results in terms of pressure curves along the tube from both the O05 test and the B05 test will therefore be presented in the following. Figure 13 contains the pressure histories at the respective sensors in the O05 and B05 tests, while Figure 14 compares the pressure histories at the pressure at the sensors before and after the tube bundle for the O05 and B05 tests. As in Section 3.2.1, the sensors were flush mounted with the roof of the internal cross-section and positioned 12.275 (P08_01), 12.285 (P08_02), 10.785 (P07_01), 10.885 (P07_02), 15.125 (P10_01) and 15.225 (P10_02) m upstream the open end of the tube (see Figure 4a). The pressure sensors were automatically triggered when the shock wave arrived at P08_01 and operated with a sampling frequency of 500 kHz.

Some preliminary observations:

- The overall trend in test B05 (Figures 13 and 14) is similar to that in test B02 (see Figures 13 and 14), but with increasing magnitudes of pressure and a less distinct 'kink' before the exponential decay. That is, the peak pressures are more or less followed by an exponential decay, with no distinct 'kink'.
- As in test B02, Figures 13b and 14a show three distinct jumps in pressure at Sensors P08 for test B05. This implies that there is an influence of both the box and the tube bundle on the pressure recorded upstream the tube bundle. The first jump in pressure is as expected and due to the increase in pressure over the shock wave, while the second and the third jump may be related to reflected pressures due to the box and the tube bundle.

Document property of CEA, issued in the framework of the agreement Tripartite Institute 2020 - F35158
Reproduction and transmission governed by the terms of the agreement

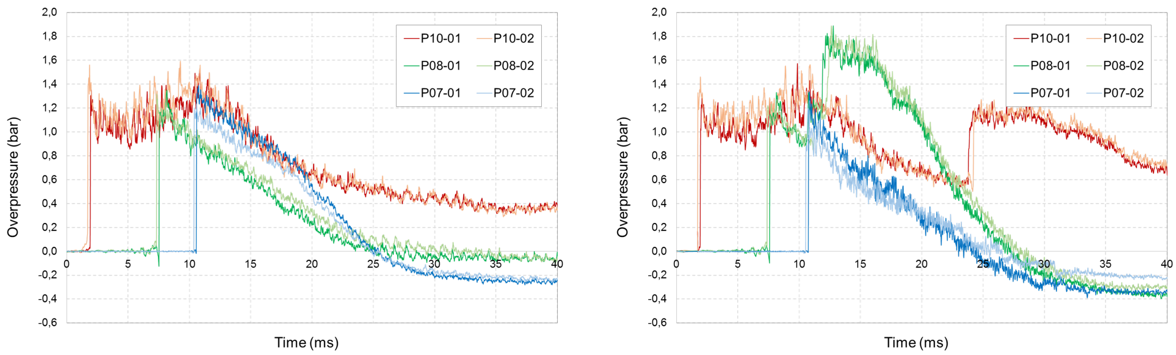

(a) (b)

Figure 13: Pressure measurements along the tube in test: (a) O05 and (b) B05. The number of sensors were limited to 6 channels in the data acquisition system and the respective sensors were positioned 12.275 (P08_01), 12.285 (P08_02), 10.785 (P07_01), 10.885 (P07_02), 15.125 (P10_01) and 15.225 (P10_02) m upstream the open end of the tube (see Figure 4a).

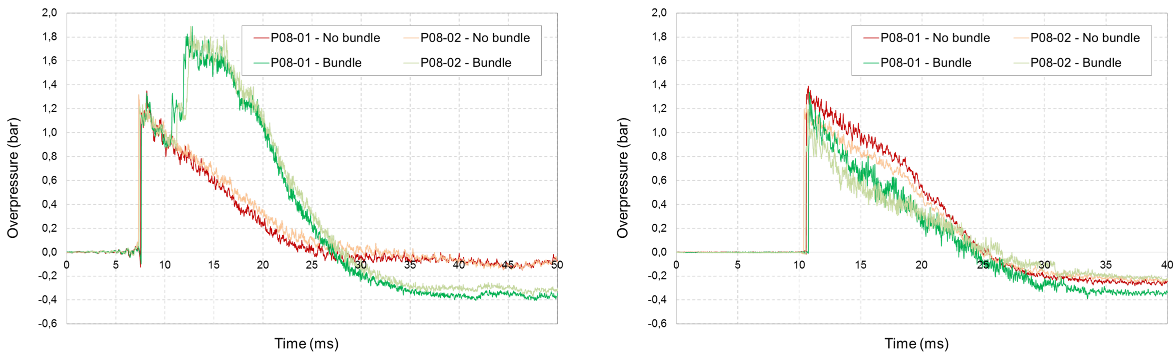

(a) (b)

Figure 14: Pressure measurements in test O05 and B05 at sensors: (a) P08 and (b) P07. The respective sensors were positioned 12.275 (P08_01), 12.285 (P08_02), 10.785 (P07_01) and 10.885 (P07_02) m upstream the open end of the tube (see Figure 4a).

Document property of CEA, issued in the framework of the agreement Tripartite Institute 2020 - F35158
Reproduction and transmission governed by the terms of the agreement

3.3.2 Schlieren vizualization of the rods and the shock wave

The images obtained from the telecentric lenses in terms of a Schlieren-like vizualization will be presented in the following. These measurements provide images of the rods motion and the shock wave propagation close to the tube bundle. The experimental results in this section will be limited to the B05 test, since test O05 was carried out with an open tube without any box or bundle.

Some preliminary observations:

- Figures 15a-15e show the initial, undeformed configuration of the rods prior to the wave impact.
- Figures 15b-15e show an almost planar shock wave on its way to the tube bundle. Similar high-speed images for test O05 show a perfectly planar shock wave. This may indicate that there has been some disturbances of the planar shock wave due to the surrounding box of the tube bundle.
- Figures 15f is more or less the exact point of impact and first interaction between the shock wave and the first row of rods in the tube bundle.
- Figures 15g-16a show that parts of the wave is reflected, parts of the wave interacts with the tube, while the remaining passes on the sides of the tube bundle.
- It also worth noting that the rods have negligible deformations until t = 7.6047 ms (see Figures 16a and 18). This may indicate that the response of the tube bundle is dominated by the drag pressure following the shock wave and not the first interaction with the shock wave itself (shock wave impact).

3.3.3 Displacement bundle

Figure 16 shows a series of images representing the dynamic response of the tube bundle. The dynamic response is obtained using subset digital image correlation (DIC) to track the displacement of the first row of bundles in test B02. Figure 11 attempts to illustrate how this subset DIC is carried out by tracing the greyscale values inside a subset throughout the entire image series (see red square in Figure 11), while Figure 12 shows the corresponding displacement of the first row of bundles in the longitudinal direction of the tube. As in Section 3.2.3, the subset DIC was carried out using an MATLAB code developed at SIMLab, NTNU.

Some preliminary observations:

- Note that all times of interest (TOI) in Figure 16 are illustrated by black markers in Figure 18. The mid-point of the first row of rods is indicated by the red marker in Figure 17.
- Figure 16a shows the point in time when the first row of rods start to move.
- Figures 16b-16c show points in time when the first row of rods are on their way to the maximum deformation.
- Figures 16d, 16e and 16f show the points in time when the first row of rods reach maximum deflection.

- Figures 16g-16o correspond to the remain times of interest (TOI) in Figure 18.
- Figures 16h-16n indicate that several rods may be in contact to each other during the test.
- Figure 18 shows that that the mid-point of the first row of rods undergoes a rapid deformation from t = 7.6047 ms (Figure 16a) until the point of maximum deflection at t = 9.7399 ms (Figure 16e), before the supporting structure of the box fails sometime in-between t = 9.9561 ms (Figure 16f) and t = 11.5237 ms (Figure 16g). The failure of the box is observed in the images as a black vertical line moving from left to right, starting at t = 11.5237 ms (Figure 16g) and continuing throughout the test. This black vertical line is the left edge of the square windows in the supporting box (see Figure 5), clearly showing that the entire box is moving from left to right inside the tube. The tube bundle has moved outside the field of view at t = 19.0372 ms (Figure 16o). The failure of the box is also evident in Figure 18, where the overall trend is that the rod displacement is more of less progressively increasing from around t = 12 ms and throughout the test (instead of elastic vibrations around a permanent deformed configuration).
- It is challenging to conclude on the influence of box failure on the pressure profiles in Figures 13 and 14, since the overall trend in test B05 is similar to that in test B02 (see Figures 13 and 14).

Document property of CEA, issued in the framework of the agreement Tripartite Institute 2020 - F35158
Reproduction and transmission governed by the terms of the agreement

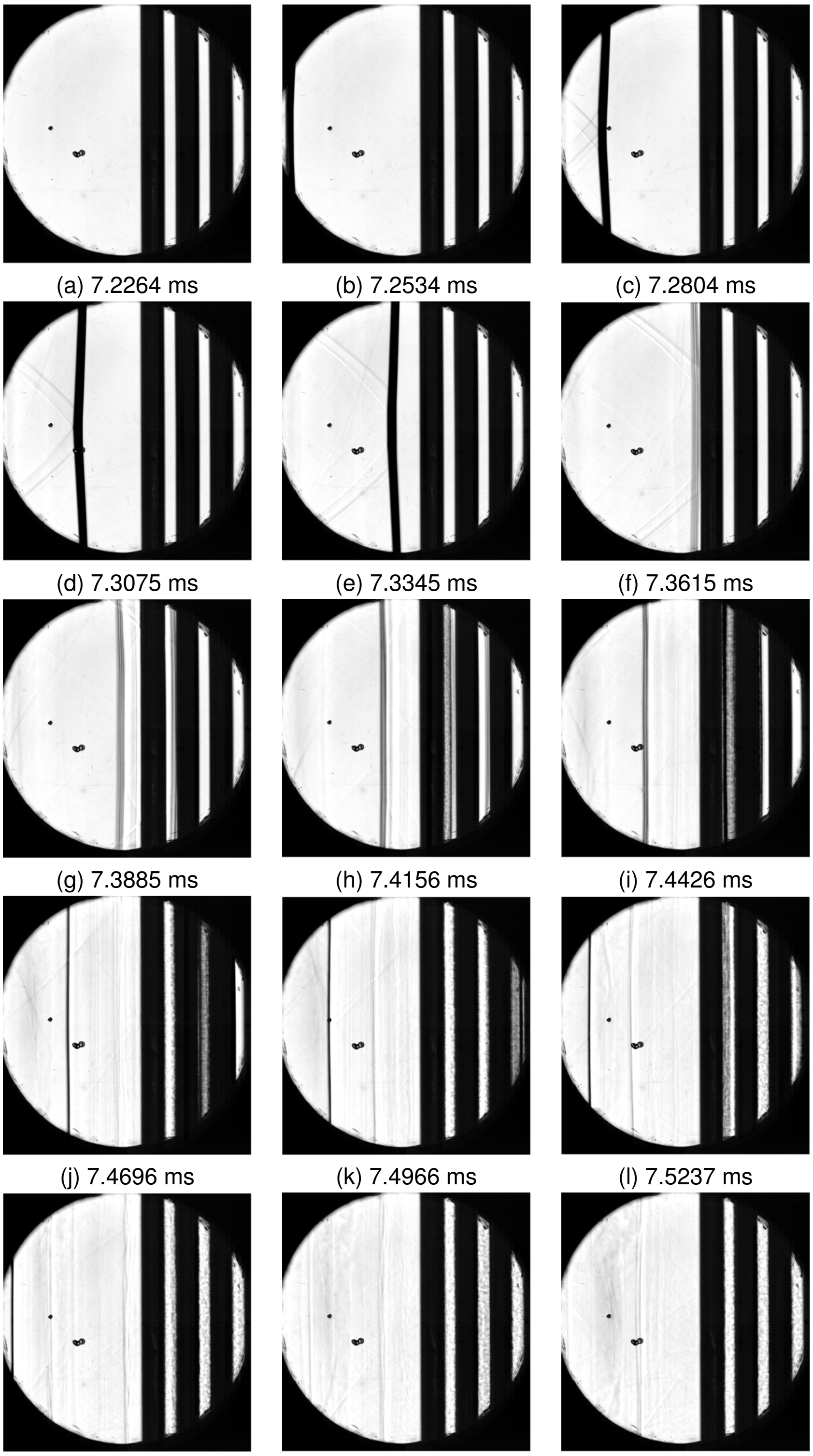

(a) 7.2264 ms (b) 7.2534 ms (c) 7.2804 ms
(d) 7.3075 ms (e) 7.3345 ms (f) 7.3615 ms
(g) 7.3885 ms (h) 7.4156 ms (i) 7.4426 ms
(j) 7.4696 ms (k) 7.4966 ms (l) 7.5237 ms
(m) 7.5507 ms (n) 7.5777 ms (o) 7.6047 ms

Figure 15: Schlieren-like vizualization in test B05 using the telecentric setup in Figures 4d, 4f and 4g. Time zero (t=0) is taken as the arrival of the shock wave at Sensor P10_02.

Document property of CEA, issued in the framework of the agreement Tripartite Institute 2020 - F35158
Reproduction and transmission governed by the terms of the agreement

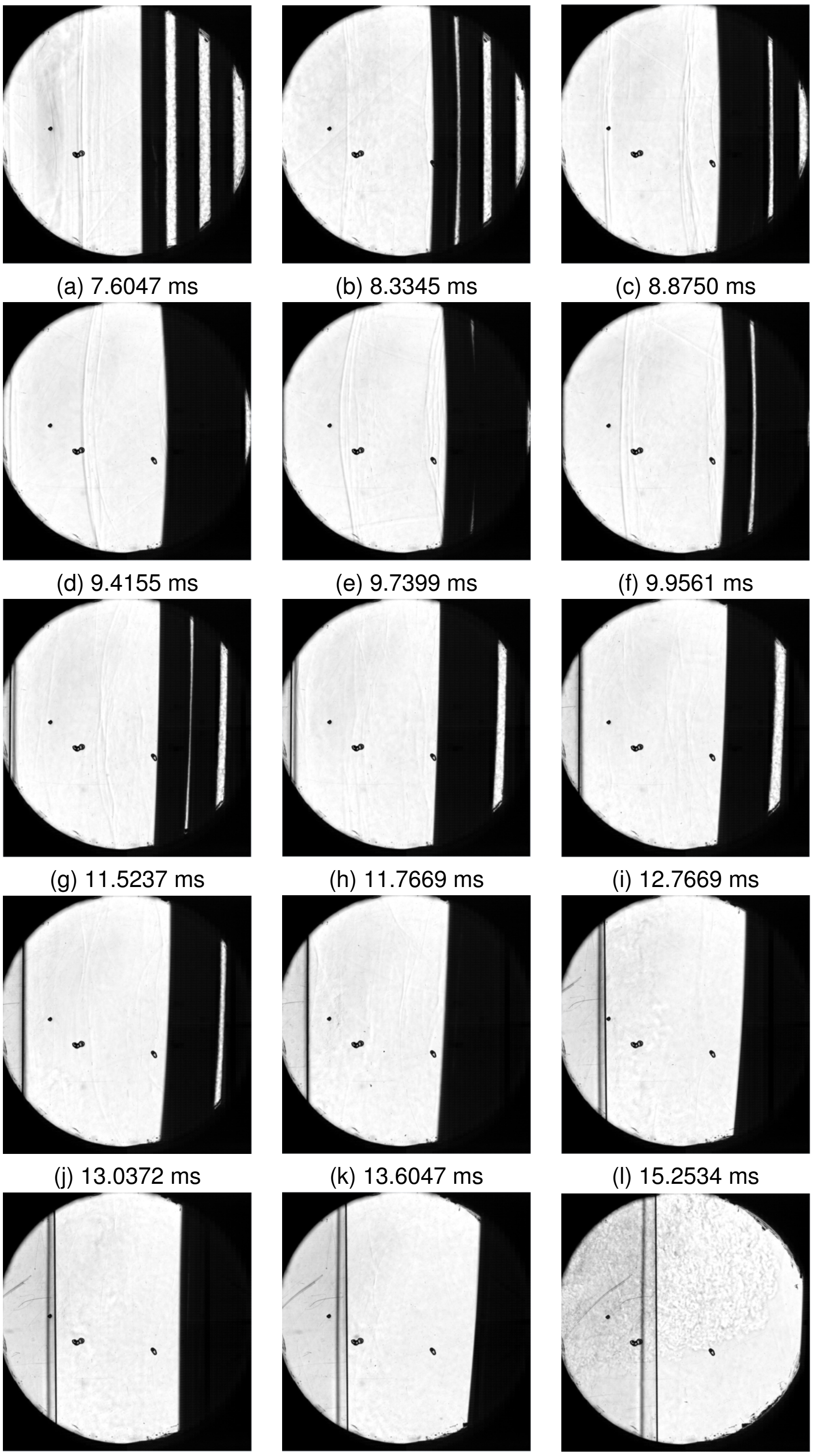

(a) 7.6047 ms (b) 8.3345 ms (c) 8.8750 ms
(d) 9.4155 ms (e) 9.7399 ms (f) 9.9561 ms
(g) 11.5237 ms (h) 11.7669 ms (i) 12.7669 ms
(j) 13.0372 ms (k) 13.6047 ms (l) 15.2534 ms
(m) 16.0101 ms (n) 16.9831 ms (o) 19.0372 ms

Figure 16: Schlieren-like vizualization in test B05 using the telecentric setup in Figures 4d, 4f and 4g. Time zero (t=0) is taken as the arrival of the shock wave at Sensor P10_02.

Document property of CEA, issued in the framework of the agreement Tripartite Institute 2020 - F35158
Reproduction and transmission governed by the terms of the agreement

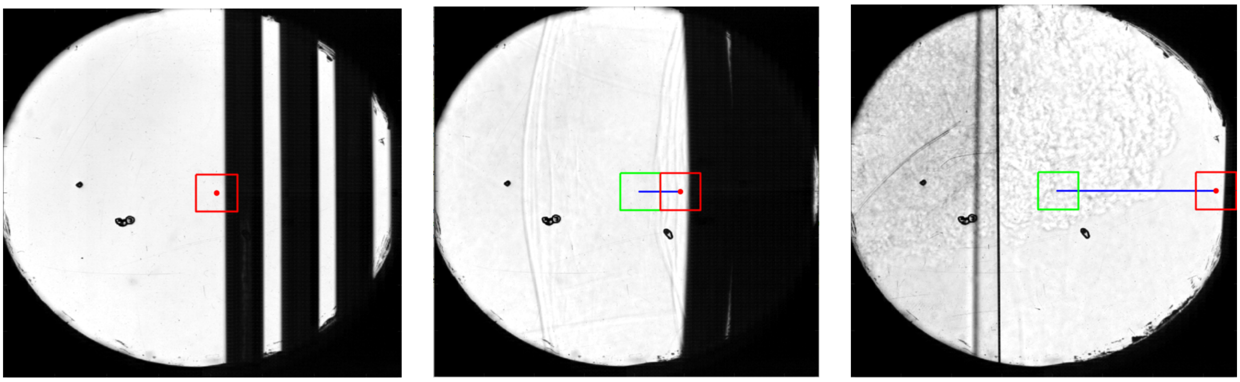

(a) (b) (c)

Figure 17: Illustration of the subset DIC carried out in MATLAB using the images from the using the telecentric setup in Figures 4d, 4f and 4g: (a) first image, (b) image corresponding to the point of maximum deformation in the first row of bundles, and (c) at the last recorded image.

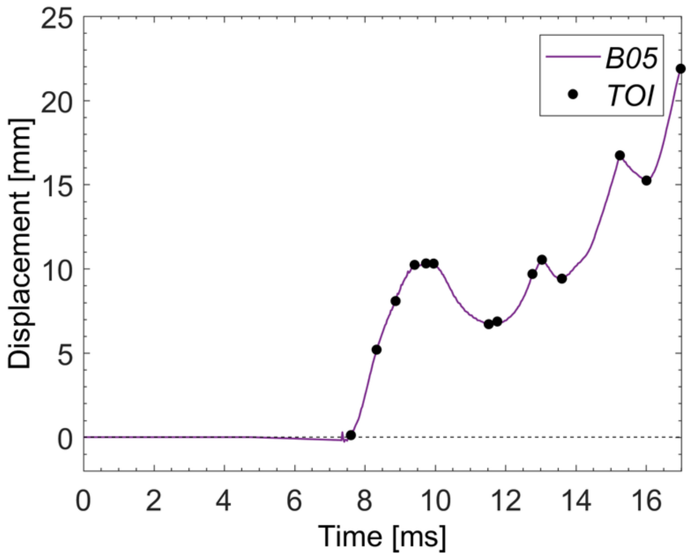

Figure 18: Dynamic response of the first row of bundles in test B05, in terms of displacement in the longitudinal axis of the tube. Time zero (t=0) is taken as the arrival of the shock wave at Sensor P10_02. Black markers corresponds to the times of interest (TOI) in Figure 16.

Document property of CEA, issued in the framework of the agreement Tripartite Institute 2020 - F35158
Reproduction and transmission governed by the terms of the agreement

4 Numerical simulations in EPX

4.1 Test interpretation with EPX

This section is dedicated to the interpretation of the tests using EUROPLEXUS Sofware (abbreviated EPX, http://www-epx.cea.fr). It consists in a two-steps methodology, where an equivalent of the pressure loading in the tube is first searched using 1D simple models, and second, the selected initial conditions are applied to a detailed 3D model implementing Fluid-Structure Interaction at local scale between the pressure wave and the rod bundle.

For the sake of simplicity in the construction of the datasets, the classical assumption for a shock tube is made that the membrane separating the high pressure chamber (called *Driver section* in Section 2.1) vanishes instantaneously when the firing pressure is exceeded. The actual membrane opening is however known to exhibit some specific dynamics, yielding inevitable discrepancies between the computed and experimental pressure signals in the tube, independently from the insertion of a specimen to test. The first subsection below is thus dedicated to the assessment of this initial deviation between simulation and experiment using 1D models, to be able afterwards to discuss the results obtained from the detailed 3D models with the simulated pressure loading. It is noticeable that some sound previous work is available through the collaboration between NTNU and the Joint Research Center of European Commission for the advanced simulation of the membrane opening transient (see [6, 7]). Resorting to such models goes beyond the scope of the current report and can be considered as prospects for the proposed work.

The equations solved for the fluid are the Euler equations for the transient evolution of an inviscid compressible fluid:

$$\begin{array}{rcl} \partial_t \rho + div\left(\rho \underline{v}\right) & = & 0 \\ \partial_t \left(\rho \underline{v}\right) + div\left(\rho \underline{v} \otimes \underline{v}\right) & = & -\underline{\nabla}\, P \\ \partial_t \left(\rho e\right) + div\left(\left(\rho e + p\right) \underline{v}\right) & = & 0 \end{array} \tag{1}$$

This set of conservation equations translates respectively the conservation of mass (ρ), momentum $(\rho \underline{v})$ and energy (ρe). It is closed by the Equation Of State for the fluid, the perfect gas relation below in the present case, giving the pressure P from the local density and internal energy:

$$P = (\gamma - 1)\,\rho e \tag{2}$$

For the 3D simulations where Fluid-Structure Interaction is taken into account, the local equation for the structural displacement q is the classical dynamic equilibrium given by, with no body force in the model:

$$\partial_{tt} q + div\left(\sigma\right) = 0 \tag{3}$$

The constitutive relation for the specimen material is basic linear elasticity:

Document property of CEA, issued in the framework of the agreement Tripartite Institute 2020 - F35158
Reproduction and transmission governed by the terms of the agreement

$$\begin{aligned} \sigma &= \lambda tr\left[\epsilon\left(q\right)\right] I + 2\mu\epsilon\left(q\right) \\ \lambda &= \frac{E\nu}{(1+\nu)(1-2\nu)} \\ \mu &= \frac{E}{2(1+\nu)} \end{aligned} \tag{4}$$

The measure of deformation ϵ is obtained from the non-linear Almansi-Euler relation accounting for finite displacements with the current configuration considered as the reference configuration:

$$\epsilon = \frac{1}{2}\left(\nabla q + \nabla^t q - \nabla^t q \cdot \nabla q\right) \tag{5}$$

The material properties for fluid and structure as well as initial conditions for the fluid are given in Tables 2 and 3. The initial conditions in the driver section depend on the considered firing pressure (2.5 or 5 bars). Cell models used in both 1D and 3D as well as additional modeling features for Fluid-Structure Interaction, boundary conditions and structural contact between rods are gathered in Table 4 (see also EPX Users' manual [8] for details). Kinematic constraints for fluids and structures are used selectively in their *coupled* or *decoupled* implementations for the optimum balance between accuracy and performance.

Table 2: Material properties and initial conditions for fluid (air, perfect gas EOS)

γ	Initial state (driver section)	Initial state (regular section)
1.4	*Firing pressure 2.5 bars* : ρ=4.1945 kg.m^{-3} P$_{ini}$=3.5473 $\times$ 10^5 Pa *Firing pressure 5 bars* : ρ=7.305 kg.m^{-3} P$_{ini}$=6.185 $\times$ 10^5 Pa	ρ=1.1777 kg.m^{-3} P$_{ini}$=9.9599 $\times$ 10^4 Pa

Table 3: Material properties for structure (polymethyl-methacrylate, linear elasticity)

ρ	E	ν
1185 kg.m^{-3}	3 GPa	0.4

Document property of CEA, issued in the framework of the agreement Tripartite Institute 2020 - F35158
Reproduction and transmission governed by the terms of the agreement

Table 4: Models for fluid, structure and their interactions

Model	EPX keyword(s)	Description
1D tube element	`TUBE`	Mixed Finite Volume (mass and energy conservation) / Finite Element (momentum conservation) 1D formulation for Eulerian pipes
3D fluid element	`CUBE`	Mixed Finite Volume (mass and energy conservation) / Finite Element (momentum conservation) 3D formulation for Eulerian hexahedra
3D solid element	`CUB8`	Fully integrated 3D formulation for Lagrangian hexahedra
Fluid boundary conditions	`LINK COUP FSR`	Rigid conditions on the boundary of the fluid domain with automatic computation of the normal direction (*coupled implementation*)
Fluid 1D-3D junction	`LINK DECO TUBM`	Superelement connecting 1 node of a TUBE element to a series of faces of CUBE elements and ensuring kinematic continuity and transport of Eulerian quantities (*decoupled master/slave implementation*)
Immersed Fluid-Structure Interaction	`LINK DECO FLSR`	Vicinity fluid node against structural facet non-penetration condition for fluid velocity with disconnected meshes (*decoupled master/slave implementation*)
Structural contact	`LINK COUP GLIS`	Node-to-facet 3D contact, defined in a symmetric way for enhanced accuracy (*coupled implementation*)

4.2 1D simulations

4.2.1 Models and results

An important step in the investigation of fluid-structure interaction (FSI) effects during the shock wave propagation through flexible bundles is an accurate description of the loading. It is therefore needed to evaluate the performance of the fluid subdomain before quantifying the FSI effects in the experiments on tube bundles presented in Section 3. The objective of this section is thus to assess the capabilities of EPX in predicting the experimental pressure wave propagation in the shock tube without the bundle. As introduced in Section 4.1, it is known that the actual opening of the membrane in the experiment once the firing pressure is exceeded exhibits a proper transient that differs from the ideal shock tube conditions. The proposed simulations implement the latter and the produced

Document property of CEA, issued in the framework of the agreement Tripartite Institute 2020 - F35158
Reproduction and transmission governed by the terms of the agreement

pressure time histories are compared to the experiments, in order to identify the differences due specifically to the membrane dynamics.

The modelling characteristics on the simulations for both firing pressure of 2.5 and 5 bars have been given in Tables 2 and 4. The mesh size is 1 cm, yielding a total number of 1820 cells for the entire tube.

The results in terms of pressure measured at sensors P10_01, P08_01 and P07_01 locations for both simulation and experiments are given in Figure 19 for 2.5 (Test O02) and 5 bars (Test O05) firing pressures.

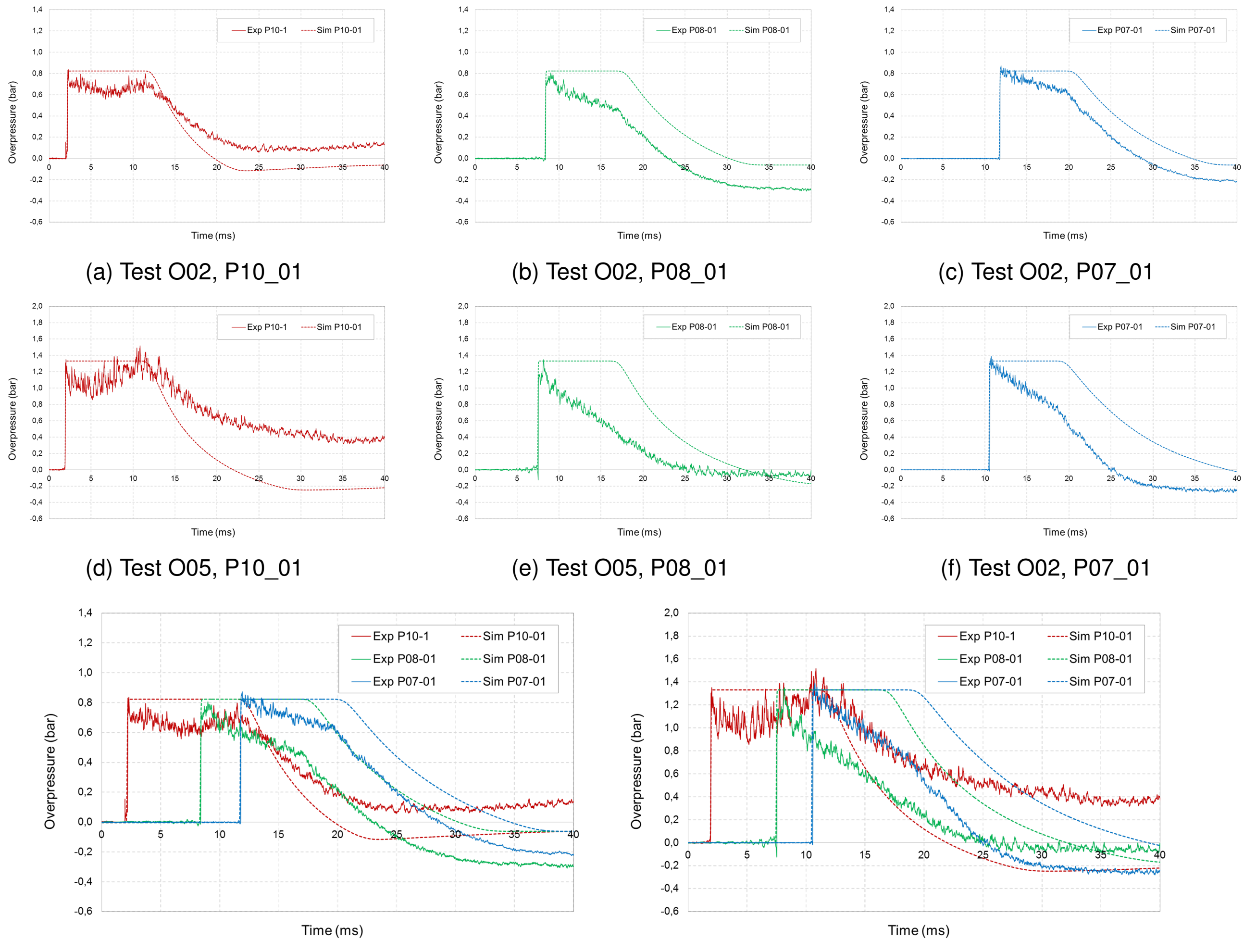

(a) Test O02, P10_01 (b) Test O02, P08_01 (c) Test O02, P07_01

(d) Test O05, P10_01 (e) Test O05, P08_01 (f) Test O02, P07_01

(g) Test O02, all three sensors (h) Test O05, all three sensors

Figure 19: Pressure measurements in open tube tests (Exp) and corresponding 1D numerical simulations (Sim). Time zero (t=0) is taken at the (instanteneous) opening of the membrane in the simulation.

4.2.2 Interpretation and comments

About the general physics of the shock

The perfect gas model and the initial conditions provided in Table 2 yield accurate overpressure levels and shock velocities for both firing pressure. The correct jumps are reproduced at the expected times along the tube. Even if the pressure evolution after the first jump is not correctly reproduced (see below), the duration of the constant state after the shock prior to the arrival of the rarefaction wave is accurately computed for all sensors. This is obviously more visible with the 2.5 bars firing pressure case, where this state is better preserved. The slope of the decreasing pressure after the arrival of the rarefaction wave is also rather well reproduced for sensors P08-01 and P07-01, stating the shape of the rarefaction wave is similar in the experiment and in the simulation. Sensor P10-01 is too close to the membrane opening and is therefore influenced by the local dynamics. Again, the 2.5 bars firing pressure case is closer to the numerical solution than the 5 bars firing pressure case, logically yielding enhanced disturbances due to membrane dynamics.

Theses results validate the chosen Equation Of State and conditions to design the most suitable equivalent theoretical shock tube to interpret the experiments.

About the shape of the pressure signal

The simulations are however unable to predict the actual experimental pressure histories throughout the tests. The numerical simulations are in agreement with the theoretical shock tube solution and are characterized by the occurrence of an immediate rise in pressure before a period of constant pressure occurs. After this constant pressure there is a decrease in the driving pressure due to the reflected rarefaction waves. The reflected rarefaction is observed as an exponential decay in pressure after the constant pressure period.

The deviations from experimental measurements confirm that some directional energy is lost in the beginning of the tests due to diaphragm opening effects. As already addressed earlier, this was expected since in reality there are some energy lost due to an initial 3D flow in the vicinity of the firing section during the diaphragm opening process. The diaphragm burst starts by tearing at the centre followed by diagonal tearing and folding back of the petals formed during the opening process. This results in a high-velocity jet and 3D flow of the driver gas originating from the expanding hole. The finite opening time causes the shock wave to travel several tube diameters before the blast wave is fully formed, and this effect is more evident at increasing firing pressures. Increasing driver pressures involves also more diaphragms of larger thicknesses resulting in a slower diaphragm opening process preventing satisfactory folding back and increased obstructed flow during the opening process. The issue related to loss of directional energy during 3D flow in the diaphragm opening process can be overcome by using a 3D model including the diaphragm, or by reducing the shock strength and delaying the reflected rarefaction wave by increasing the driver length and reducing the firing pressure to obtain the experimental pressure profile in the vicinity of the test specimen. Still, it must be emphasized that increasing the driver length and reducing the firing pressure will alter the physics of the wave pattern upstream the test specimen. A more detailed investigation of the diaphragm opening process is considered beyond the scope of this report. Modelling and simulation of the diaphragm

Document property of CEA, issued in the framework of the agreement Tripartite Institute 2020 - F35158
Reproduction and transmission governed by the terms of the agreement

opening process would also require a characterization of the Melinex material. The numerical model assuming an instantaneous diaphragm burst is therefore considered sufficient for qualitative studies on the influence of FSI effects on the dynamic response of the tube bundles.

4.3 3D simulations

4.3.1 3D numerical model

The 3D model is composed of the association of a 1D representation of the shock tube similar to that introduced in the previous section, and of a detailed 3D representation in the vicinity of the specimen of the supporting frame, the actual rod bundle and the fluid domain. The 1D shock tube model suggests that the same differences as before between the experimental and numerical pressure waves impacting the bundle will be encountered, due to the effects of the membrane opening dynamics still not accounted for. This will require some discernment to properly isolate what comes from the interaction of the wave with the specimen and what is related to the initial variations in the shape of the incoming wave.

The model is finally described in Figure 20, displaying the global mesh, with both tube parts and full 3D part, connected together through 1D-3D junction surfaces. The 3D domain is composed of 2.435.152 hexahedral cells for the fluid and 214.400 hexahedral cells for the rods. The cell size for the fluid mesh in the vicinity of the rod bundle is chosen so that there are at least 3 fluid nodes between two rods in a horizontal section (see Figure 20-c). Each rod section has 8 cells along one diameter, to have an accurate bending behaviour with fully integrated Finite Elements, requested for numerical stability. All the geometric details of the supporting box are modelled, from the bevels to the lateral windows. Its walls are assumed perfectly rigid and clamped. The rods are clamped at their extremities, which accounts for the part inserted inside the bottom and top walls of the box. The material used for the rods has been given in Table 3. Potential contact between rods is managed, as introduced in Section 4.1.

Document property of CEA, issued in the framework of the agreement Tripartite Institute 2020 - F35158
Reproduction and transmission governed by the terms of the agreement

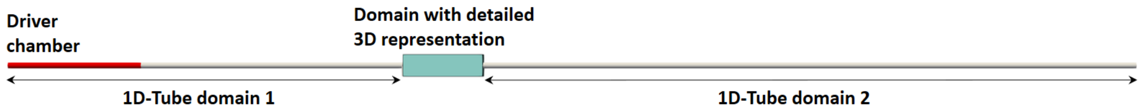

(a) Global model, connecting 1D-Tube domains to a 3D detailed domain

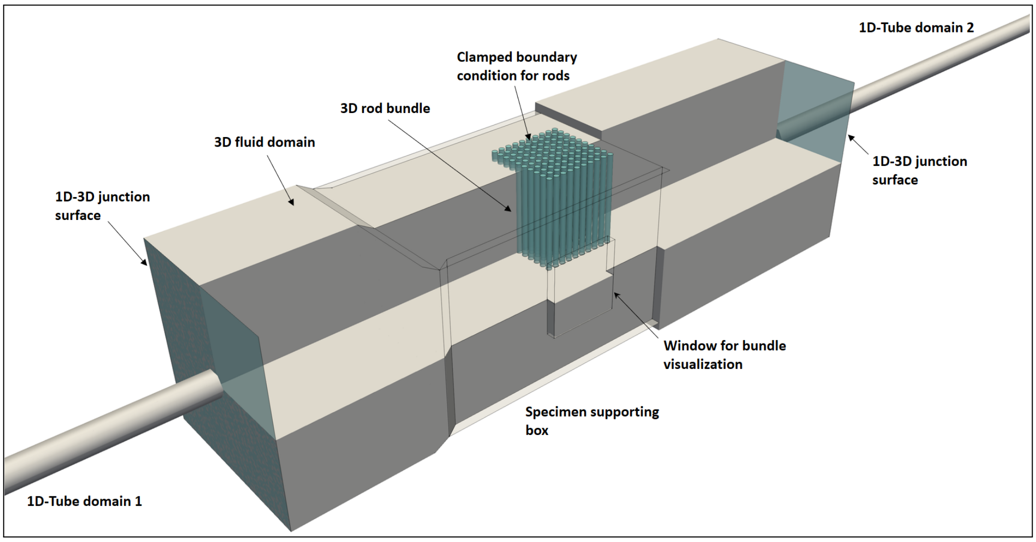

(b) Zoom on the 3D detailed domain

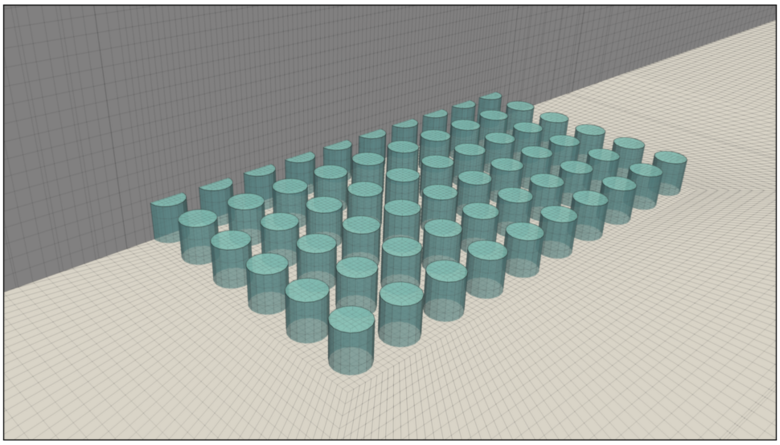

(c) Zoom on the mesh for fluid and structure in the bundle area, rods cut for visibility

Figure 20: 3D fluid-structure model for EPX

Document property of CEA, issued in the framework of the agreement Tripartite Institute 2020 - F35158
Reproduction and transmission governed by the terms of the agreement

4.3.2 Results for firing pressure 2.5 bars

The pressure waves propagation in the detailed 3D domain is given in Figures 21 and 22, with a zoom on the bundle in the latter.

The bundle motion and rods velocity are shown in Figure 23. Contact between rods is identified when stress waves start to travel inside the contacting rods in addition to the deformation arising from the fluid pressure loading, yielding a significantly more disturbed velocity field along the rods.

The Schlieren representation of the density gradient combined with Fluid-Structure Interaction, in a format matching the experimental pictures from the window section of the tube, are given in Figure 24.

Finally, Figure 25 provides the comparison between pressure evolution for Sensors P08-01 and P07-01 in the simulation and in the experiment, whereas Figure 26 displays the computed displacement of the first row of the bundle, compared to the measures given in Figure 12. In the latter, the displacements is given for 3 differents rods within the row (Rod 1 being the corner rod close to the window and Rod 5 the one of the central rods closest to the window) and the minimum is taken to compare to experiment. The experimental curve is also shifted in time to match the arrival of the wave of the bundle in the simulation.

Document property of CEA, issued in the framework of the agreement Tripartite Institute 2020 - F35158
Reproduction and transmission governed by the terms of the agreement

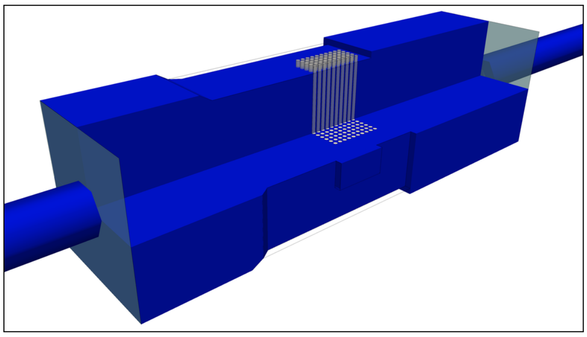

(a) Initial state

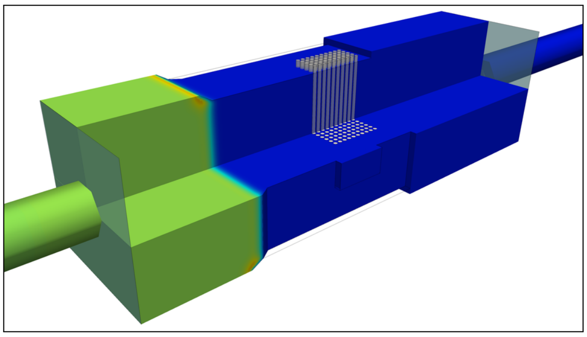

(b) Time = 9.5 ms ; the shock wave enters the 3D fluid domain

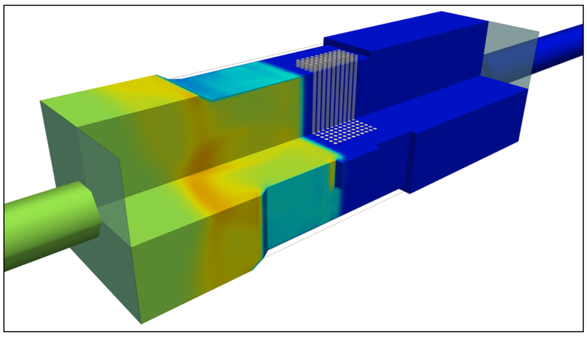

(c) Time = 10 ms ; the wave is slightly focused and diffracted when entering the bundle supporting structure

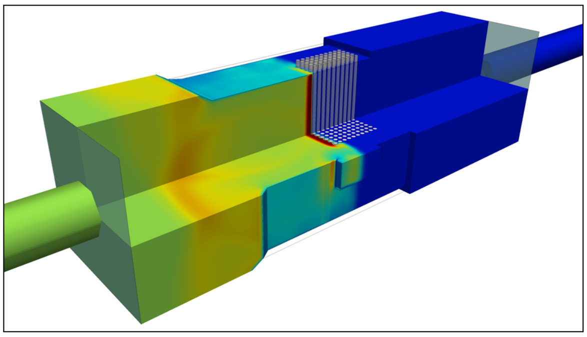

(d) Time = 10.1 ms ; interaction of the incoming wave with the bundle

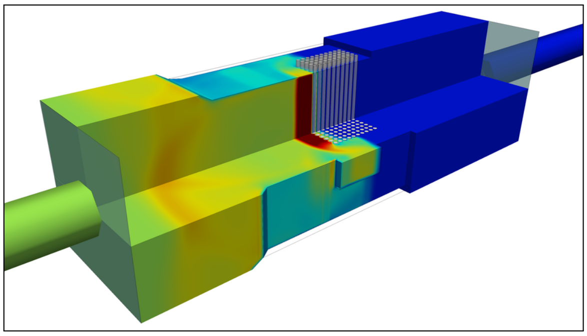

(e) Time = 10.2 ms

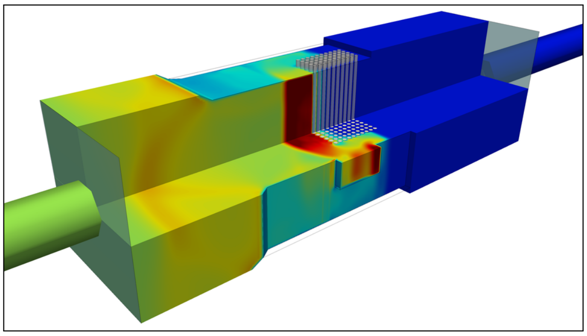

(f) Time = 10.3 ms ; the incoming wave travels preferentially in the bypasses around the bundle and reflects on the wall of the window in the supporting structure

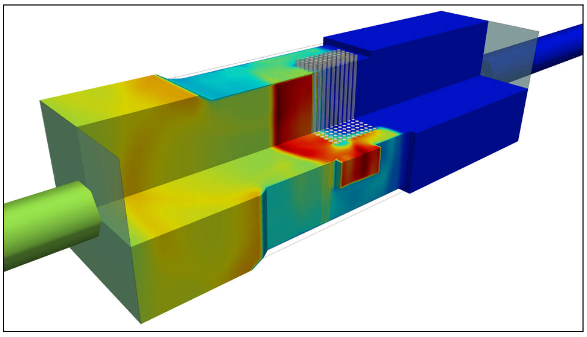

(g) Time = 10.4 ms

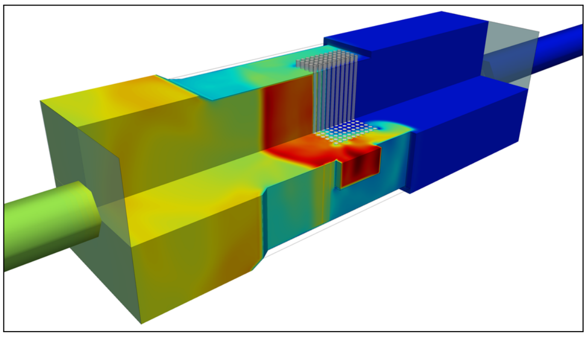

(h) Time 10.5 ms

Figure 21: Firing pressure 2.5 bars, pressure field, full 3D fluid domain

Document property of CEA, issued in the framework of the agreement Tripartite Institute 2020 - F35158
Reproduction and transmission governed by the terms of the agreement

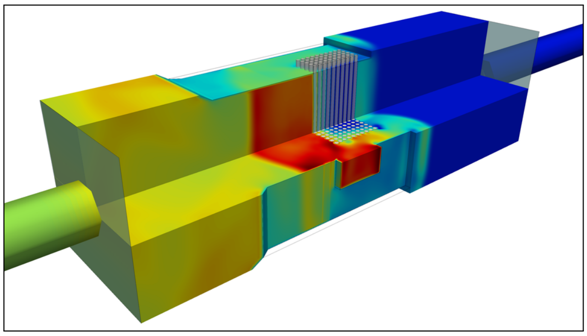

(i) Time = 10.6 ms ; the transmitted waves (through by-passes and bundle) exit the bundle area and the reflected wave propagates inf the opposite direction

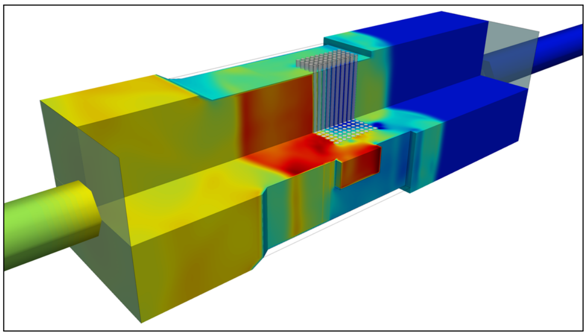

(j) Time = 10.7 ms

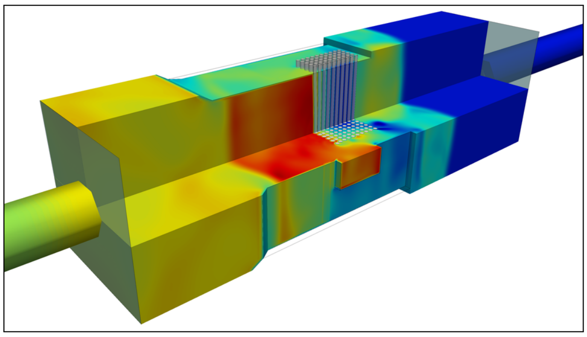

(k) Time = 10.8 ms

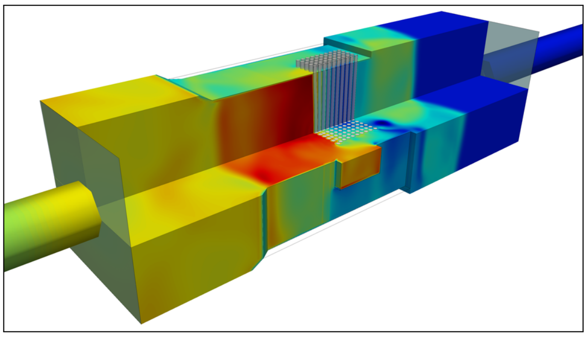

(l) Time = 10.9 ms

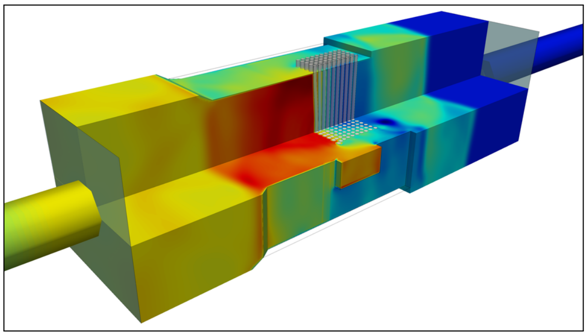

(m) Time = 11.5 ms ; the transmitted waves are almost recombined into a plane wave

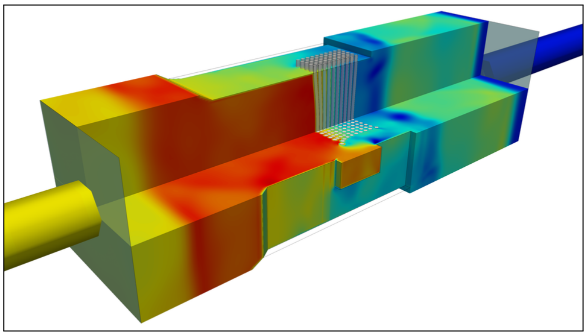

(n) Time = 12 ms ; the transmitted and reflected plane waves exit the 3D fluid domain

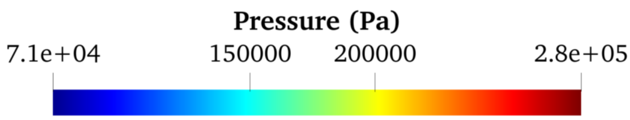

Figure 21: Firing pressure 2.5 bars, pressure field, full 3D fluid domain (continued)

Document property of CEA, issued in the framework of the agreement Tripartite Institute 2020 - F35158
Reproduction and transmission governed by the terms of the agreement

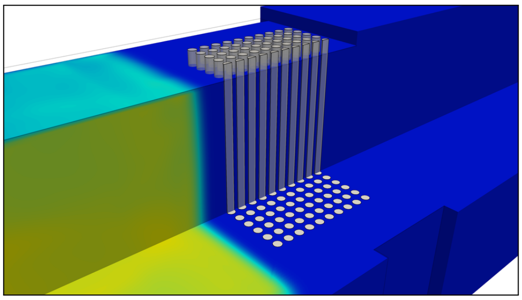

(a) Time = 10 ms

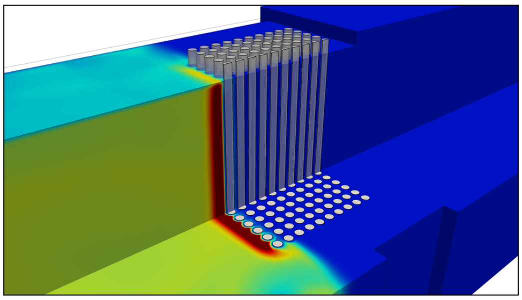

(b) Time = 10.1 ms ; generation of the quasi-plane reflected wave

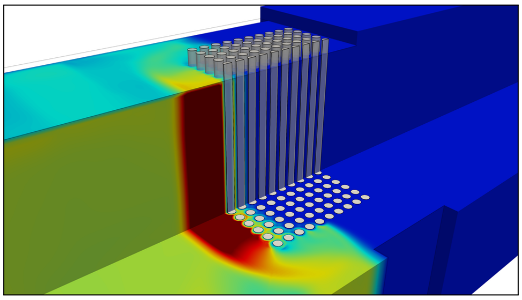

(c) Time = 10.2 ms

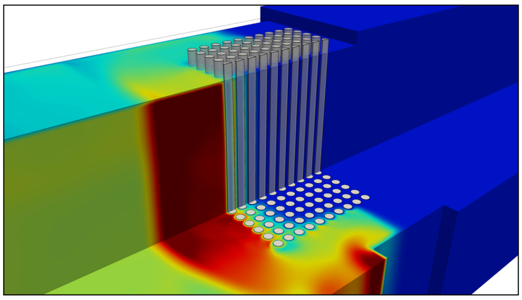

(d) Time = 10.3 ms

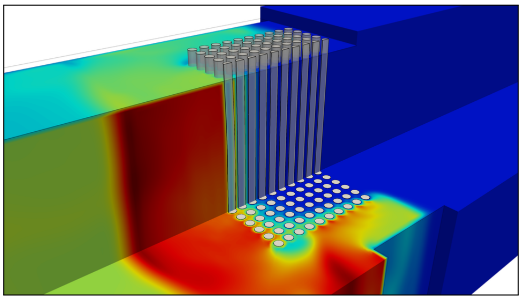

(e) Time = 10.4 ms ; lateral wave impacting the bundle after reflection on the wall of the window in the supporting structure ; quasi-homogeneous deformation of the first row of the bundle so far

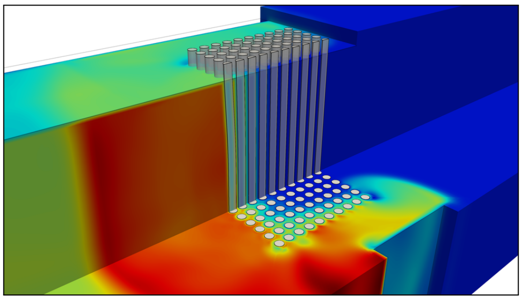

(f) Time = 10.5 ms

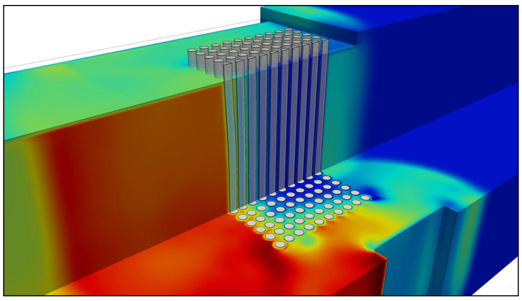

(g) Time = 10.6 ms

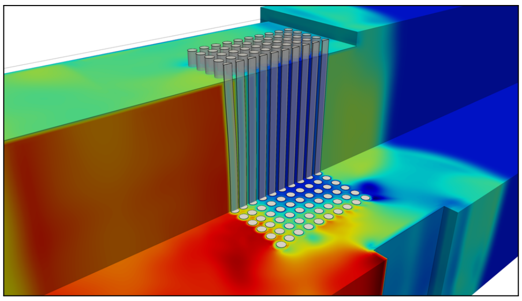

(h) Time = 10.7 ms ; transmitted waves exit the bundle ; individual displacement of the corner rod of the first row due to secondary lateral wave impact

Figure 22: Firing pressure 2.5 bars, pressure field, zoom on rod bundle

Document property of CEA, issued in the framework of the agreement Tripartite Institute 2020 - F35158
Reproduction and transmission governed by the terms of the agreement

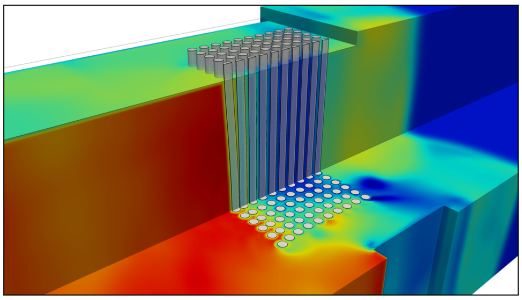

(i) Time = 10.8 ms

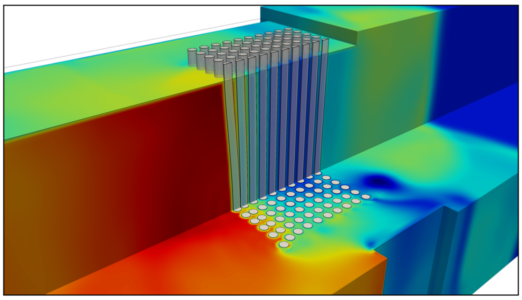

(j) Time : 10.9 ms

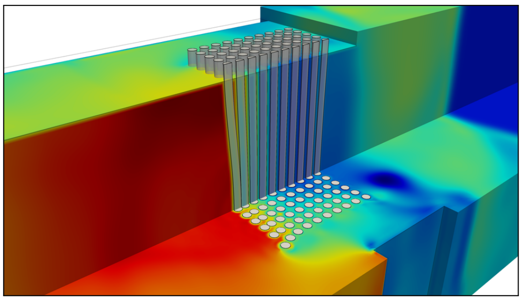

(k) Time = 11.5 ms

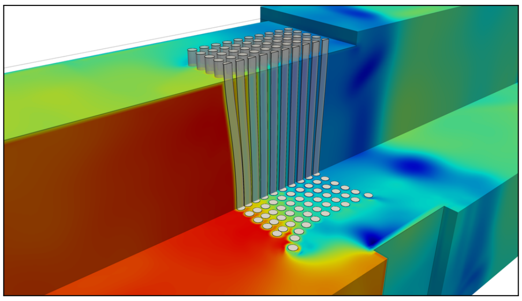

(l) Time = 12 ms ; pressure propagates inside the bundle ; complex rod motion due to multiple waves

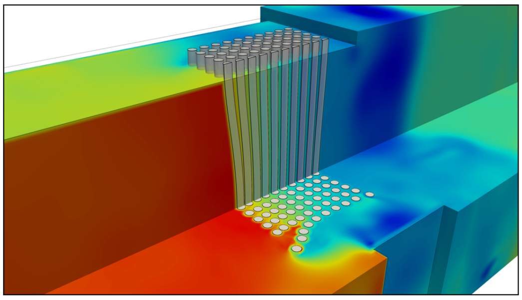

(m) Time = 12.5 ms

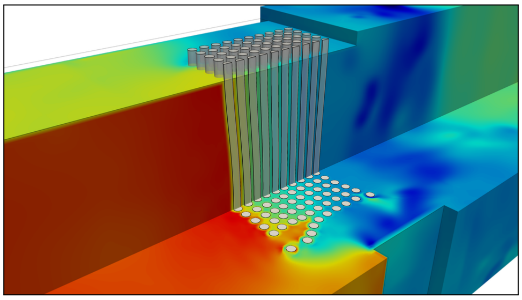

(n) Time = 13 ms

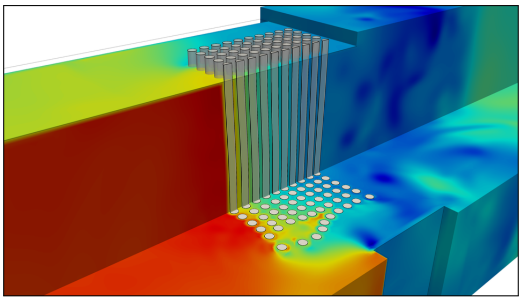

(o) Time = 13.5 ms

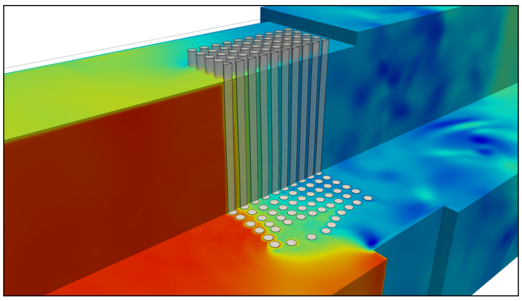

(p) Time = 14 ms ; particular displacement of the entire lateral row in response to multiple dynamic loadings

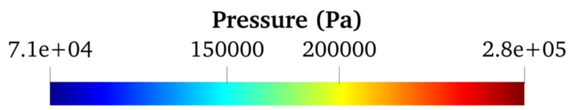

Figure 22: Firing pressure 2.5 bars, pressure field, zoom on rod bundle (continued)

Document property of CEA, issued in the framework of the agreement Tripartite Institute 2020 - F35158
Reproduction and transmission governed by the terms of the agreement

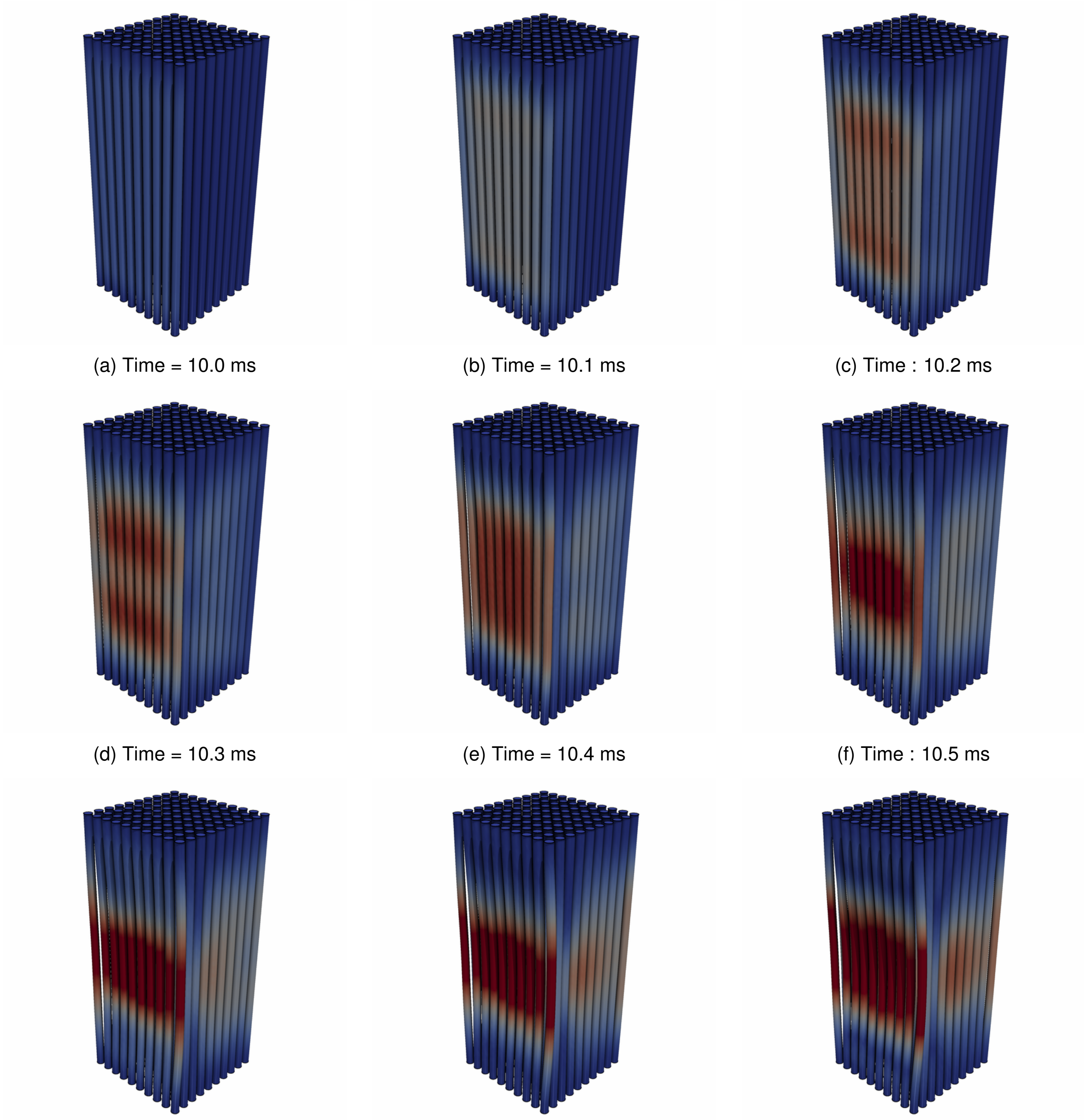

(a) Time = 10.0 ms
(b) Time = 10.1 ms
(c) Time : 10.2 ms
(d) Time = 10.3 ms
(e) Time = 10.4 ms
(f) Time : 10.5 ms
(g) Time = 10.6 ms
(h) Time = 10.7 ms
(i) Time : 10.8 ms

Figure 23: Firing pressure 2.5 bars, bundle motion and rod velocities

Document property of CEA, issued in the framework of the agreement Tripartite Institute 2020 - F35158
Reproduction and transmission governed by the terms of the agreement

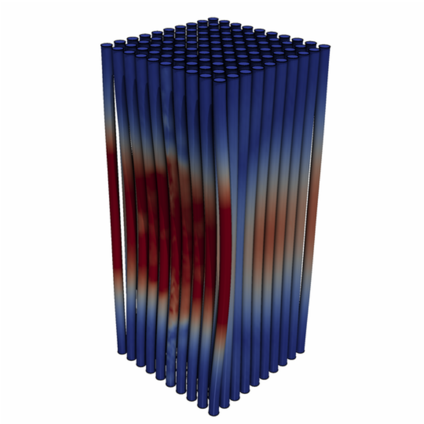

(j) Time = 10.9 ms ; contact occurs between rods in the middle of the first two rows of the bundle

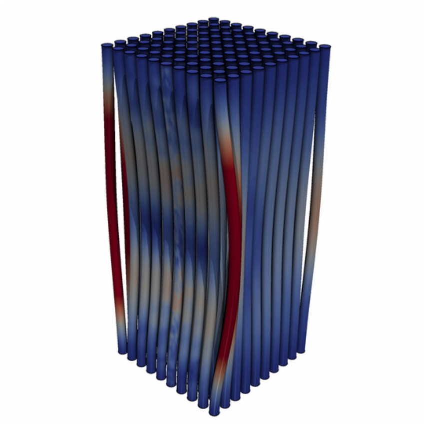

(k) Time = 11.5 ms

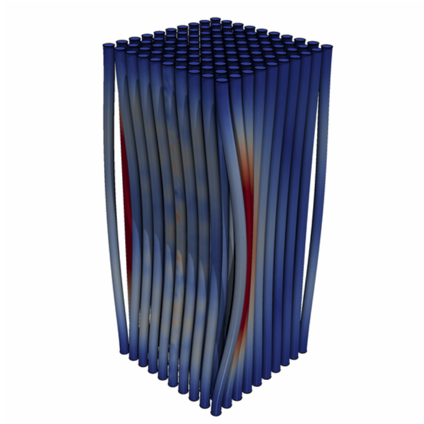

(l) Time : 12 ms

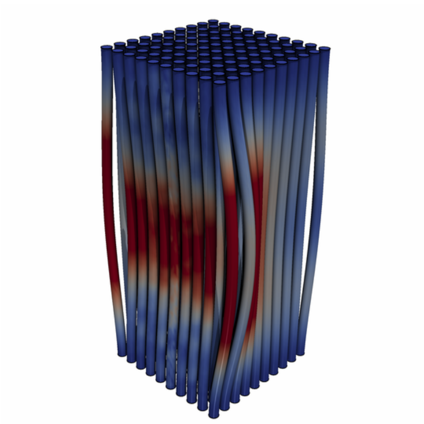

(m) Time = 12.5 ms

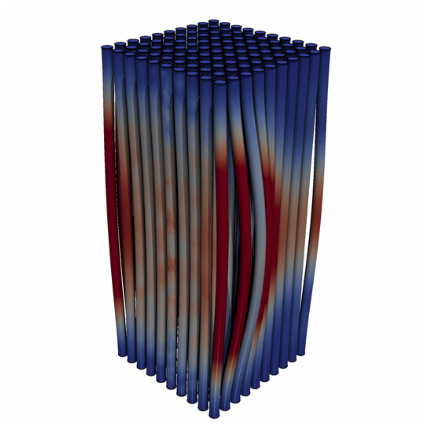

(n) Time = 13 ms ; significant individual motion of the first lateral rows of the bundle due to combined pressure loadings

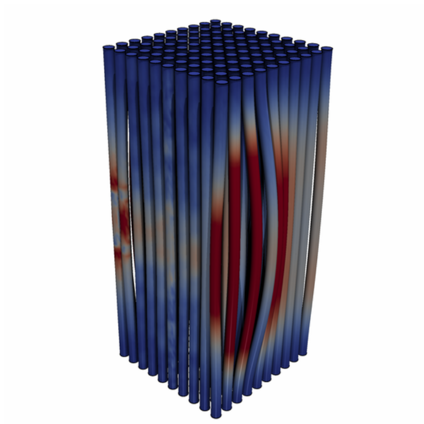

(o) Time : 13.5 ms

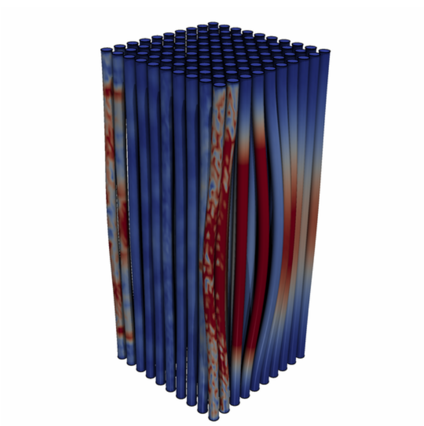

(p) Time = 14 ms ; contact occurs between rods of the lateral rows of the bundle

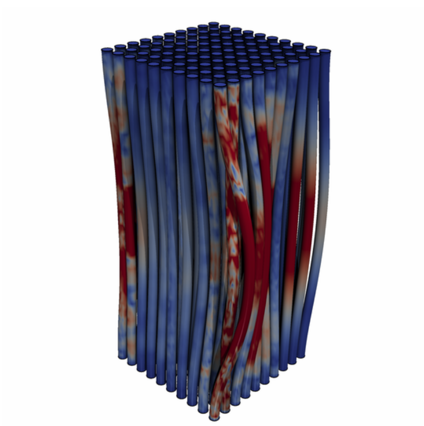

(q) Time = 17 ms ; complex motion with multiple contacts for the lateral rows of the bundle

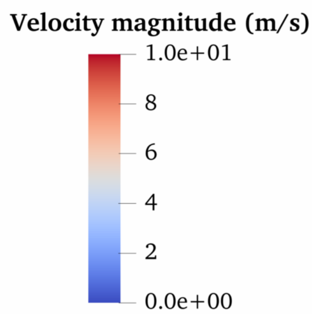

Figure 23: Firing pressure 2.5 bars, bundle motion and rod velocities (continued)

Document property of CEA, issued in the framework of the agreement Tripartite Institute 2020 - F35158
Reproduction and transmission governed by the terms of the agreement

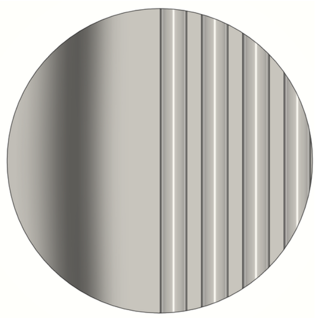

(a) Time = 10 ms

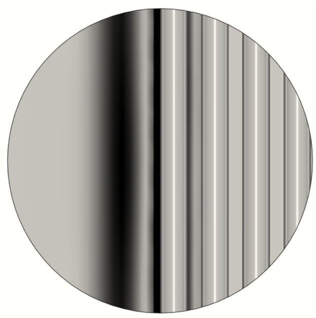

(b) Time = 10.1 ms

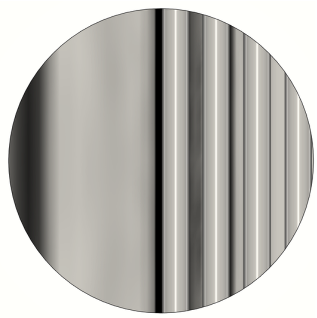

(c) Time : 10.2 ms

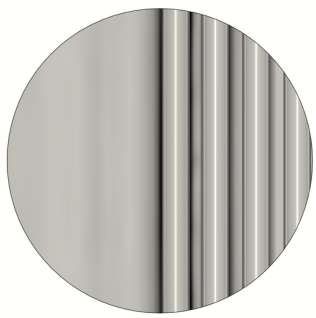

(d) Time = 10.3 ms

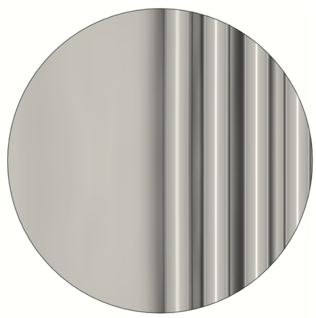

(e) Time = 10.4 ms

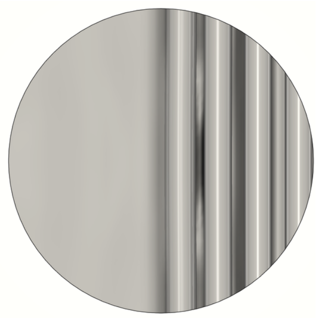

(f) Time : 10.5 ms

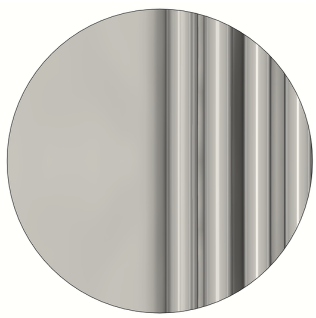

(g) Time = 10.6 ms

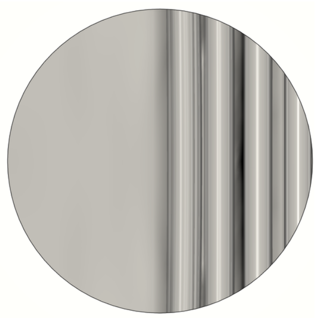

(h) Time = 10.7 ms

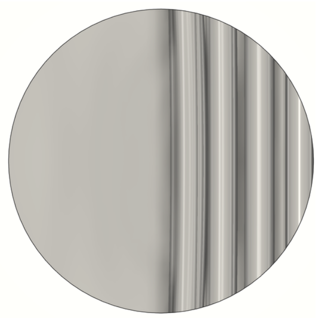

(i) Time : 10.8 ms

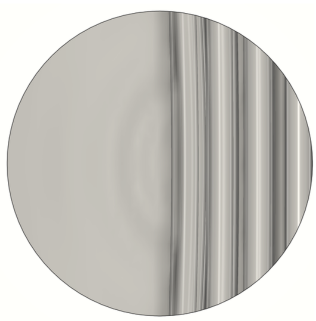

(j) Time = 10.9 ms

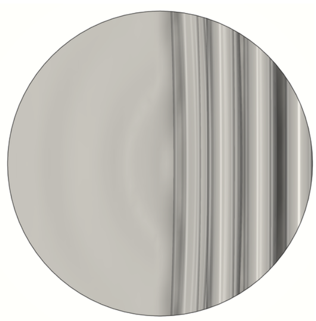

(k) Time = 11.5 ms

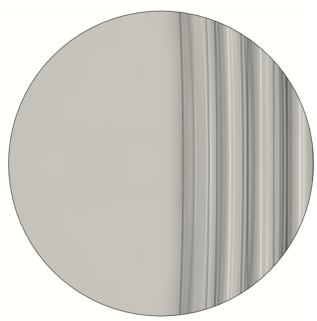

(l) Time : 12 ms

Figure 24: Firing pressure 2.5 bars, Schlieren representation for fluid density gradient and bundle motion through visualization window

Document property of CEA, issued in the framework of the agreement Tripartite Institute 2020 - F35158
Reproduction and transmission governed by the terms of the agreement

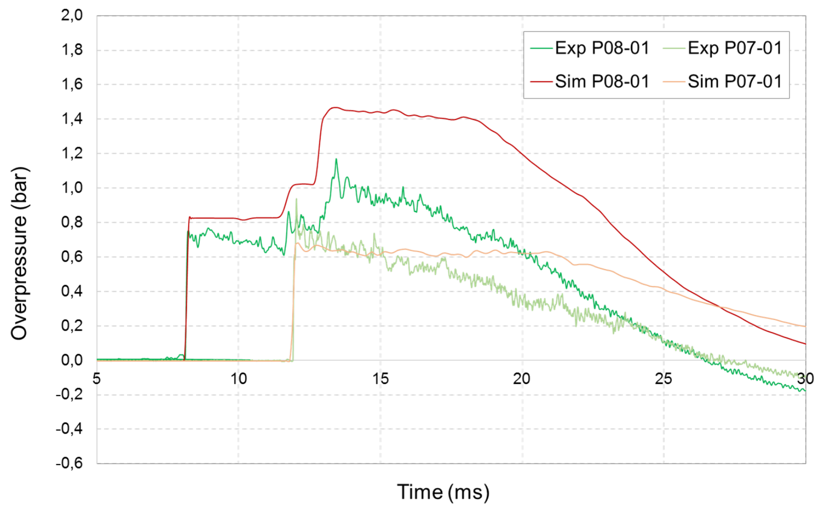

Figure 25: Firing pressure 2.5 bars, pressure evolution for Sensors P08-01 and P07-01

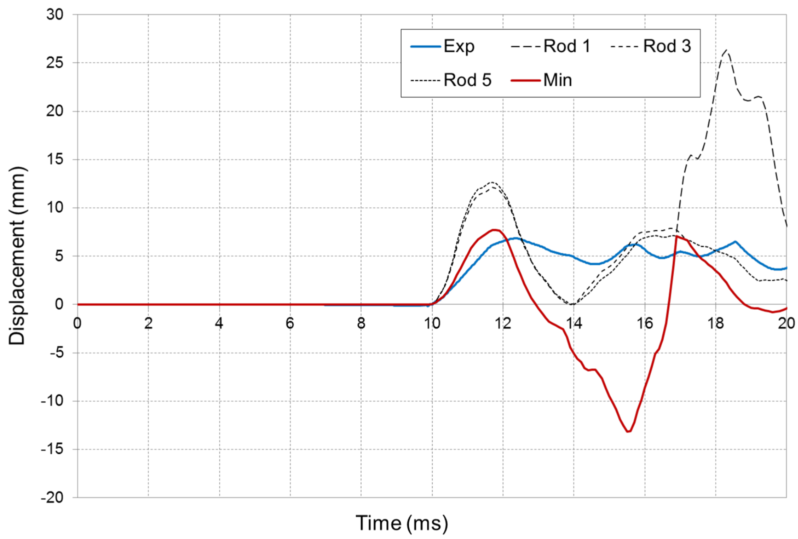

Figure 26: Firing pressure 2.5 bars, displacement of the first row of the bundle

Document property of CEA, issued in the framework of the agreement Tripartite Institute 2020 - F35158
Reproduction and transmission governed by the terms of the agreement

4.3.3 Results for firing pressure 5 bars

Results for pressure waves propagation are now given in Figures 27 and 28. The phenomenology is close to the case with 2.5 bars firing pressure. The significant differences are related to the incoming and transmitted waves travelling faster, whereas the wave reflected on the bundle travels slower than in the previous situation. The dynamic response of the bundle is also logically enhanced by the higher pressure.

This is confirmed by the bundle velocity display and Schlieren representation given in Figures 29 and 30.

Finally, Figure 31 provides again the comparison between pressure evolution for Sensors P08-01 and P07-01 in the simulation and in the experiment and Figure 32 displays the computed displacement of the first row of the bundle, compared to the measures given in Figure 18, with the same conventions as for the 2.5 bars firing pressure case. In the current case, the increase of the experimental displacement after 14 ms is obviously related the failure of the supporting box and cannot be correlated to the simulation.

Document property of CEA, issued in the framework of the agreement Tripartite Institute 2020 - F35158
Reproduction and transmission governed by the terms of the agreement

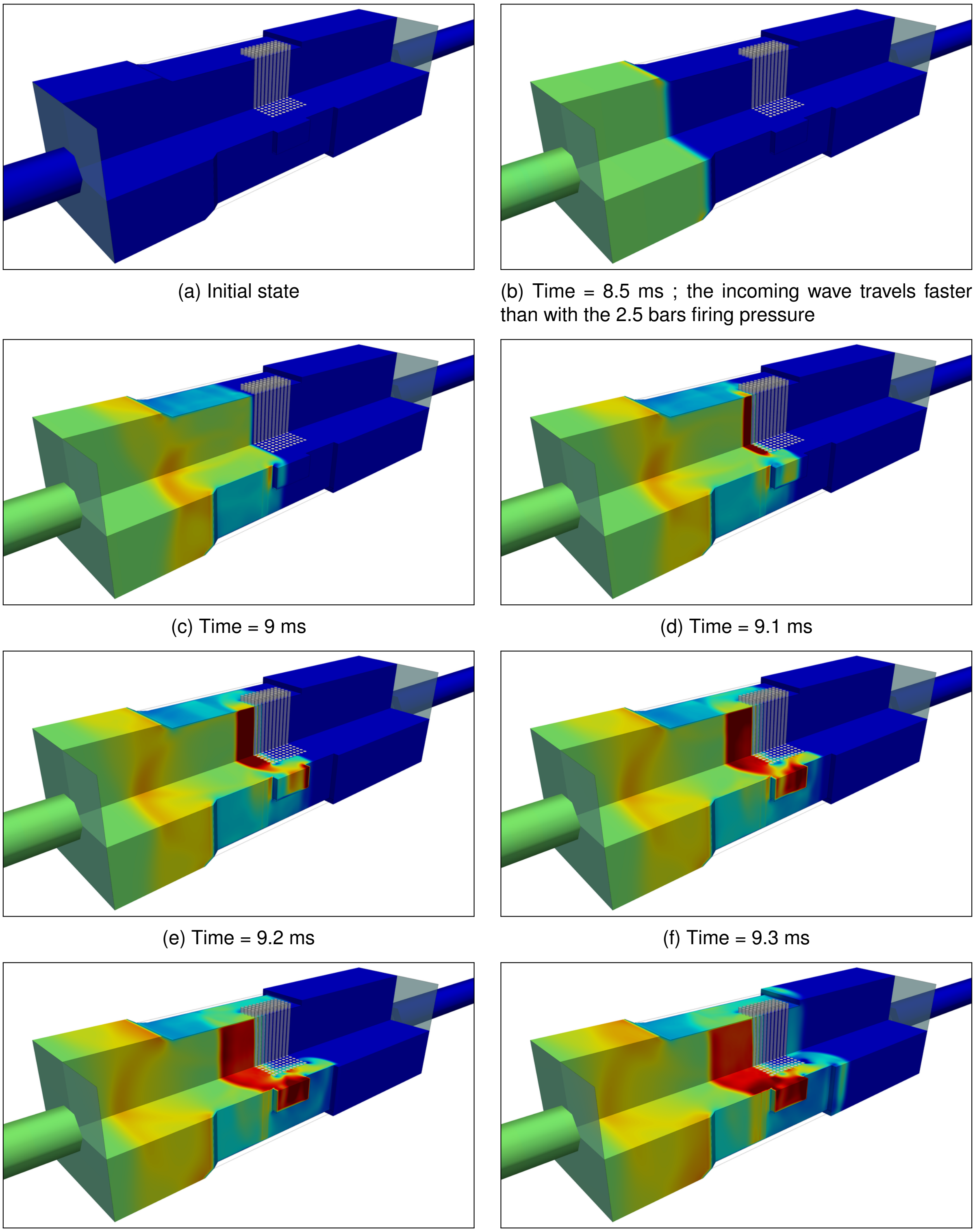

(a) Initial state

(b) Time = 8.5 ms ; the incoming wave travels faster than with the 2.5 bars firing pressure

(c) Time = 9 ms

(d) Time = 9.1 ms

(e) Time = 9.2 ms

(f) Time = 9.3 ms

(g) Time = 9.4 ms

(h) Time 9.5 ms

Figure 27: Firing pressure 5 bars, pressure field, full 3D fluid domain

Document property of CEA, issued in the framework of the agreement Tripartite Institute 2020 - F35158
Reproduction and transmission governed by the terms of the agreement

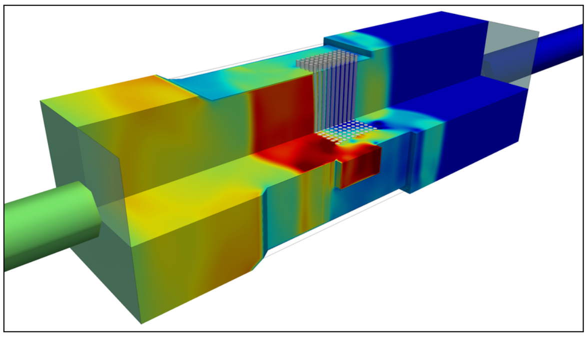

(i) Time = 9.6 ms

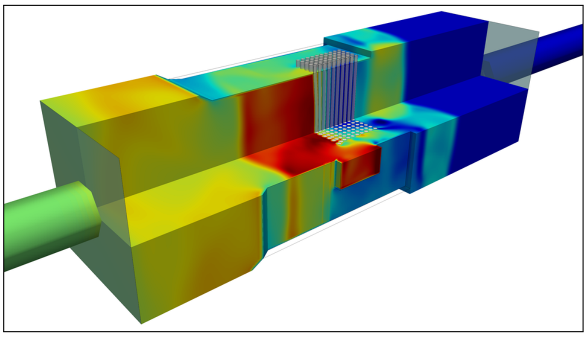

(j) Time = 9.7 ms

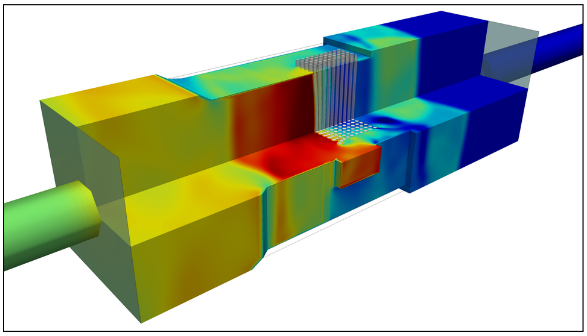

(k) Time = 9.8 ms

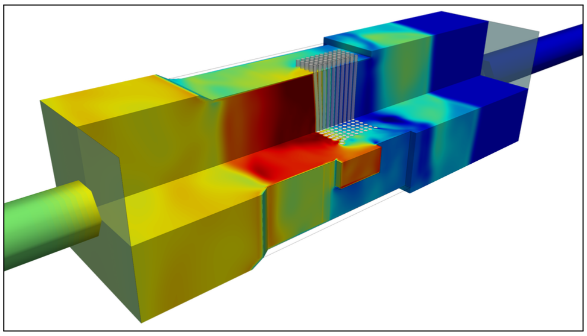

(l) Time = 9.9 ms

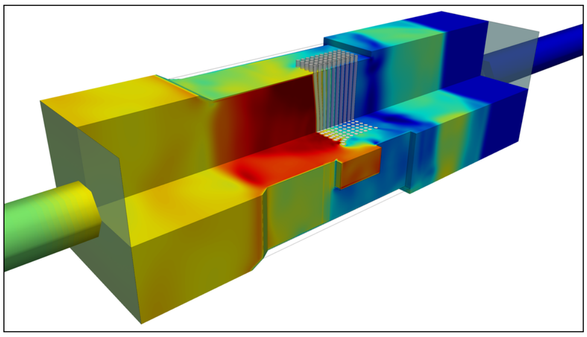

(m) Time = 10.5 ms

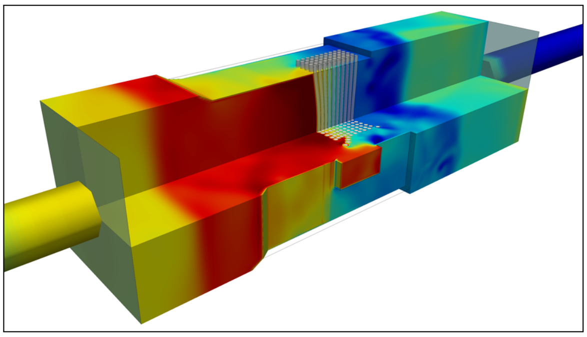

(n) Time = 11 ms ; the transmitted and reflected plane waves exit the 3D fluid domain, the reflected wave travels slower than with the 2.5 bars firing pressure

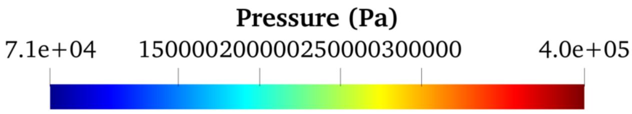

Figure 27: Firing pressure 5 bars, pressure field, full 3D fluid domain (continued)

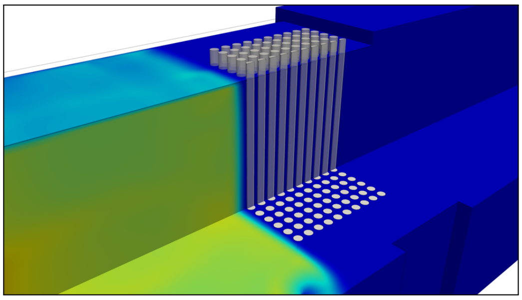

(a) Time = 9 ms

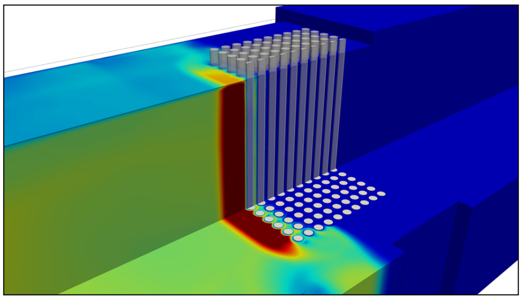

(b) Time = 9.1 ms

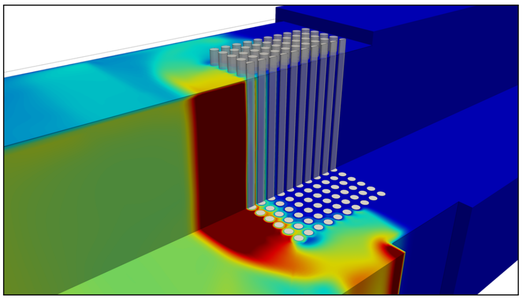

(c) Time = 9.2 ms

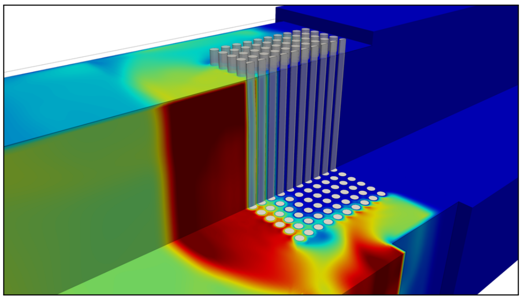

(d) Time = 9.3 ms

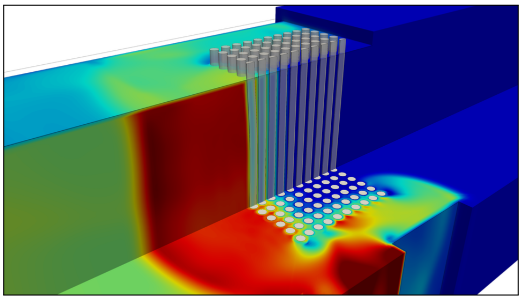

(e) Time = 9.4 ms

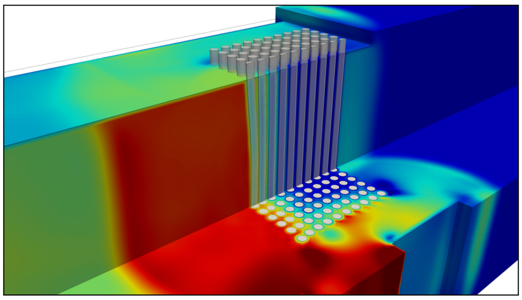

(f) Time = 9.5 ms

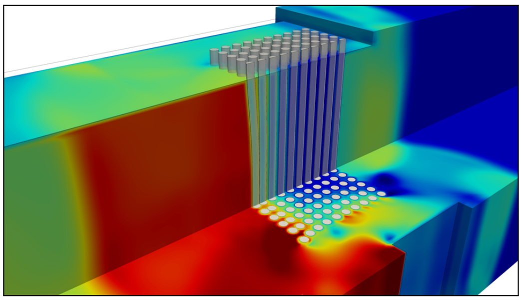

(g) Time = 9.6 ms

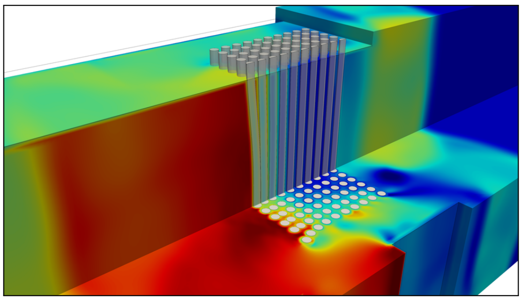

(h) Time = 9.7 ms

Figure 28: Firing pressure 5 bars, pressure field, zoom on rod bundle

Document property of CEA, issued in the framework of the agreement Tripartite Institute 2020 - F35158
Reproduction and transmission governed by the terms of the agreement

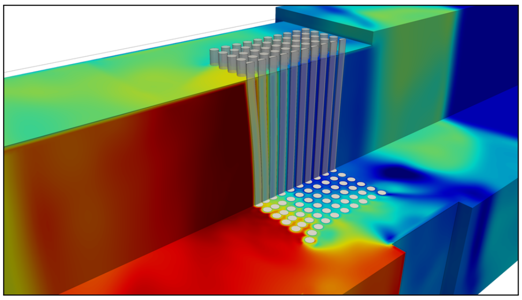

(i) Time = 9.8 ms

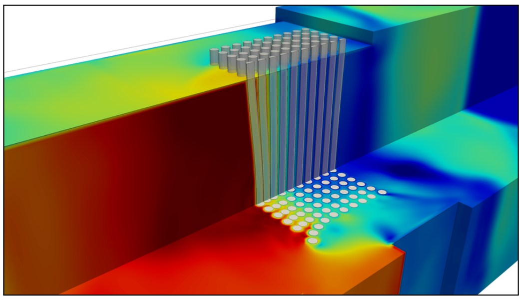

(j) Time : 9.9 ms

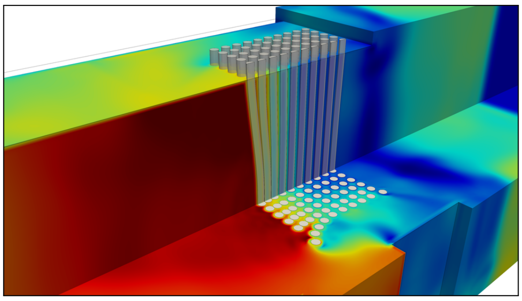

(k) Time = 10.5 ms

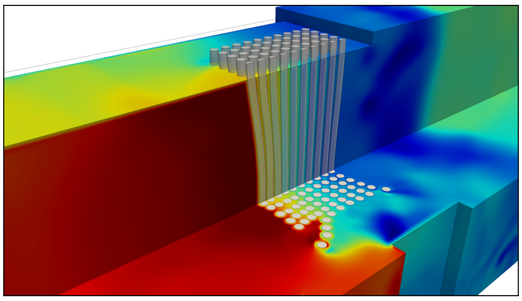

(l) Time = 11 ms

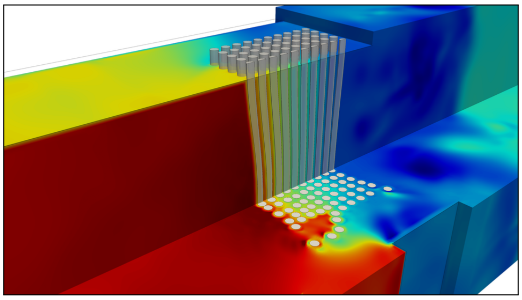

(m) Time = 11.5 ms

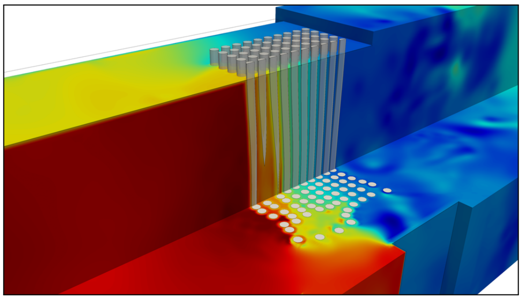

(n) Time = 12 ms

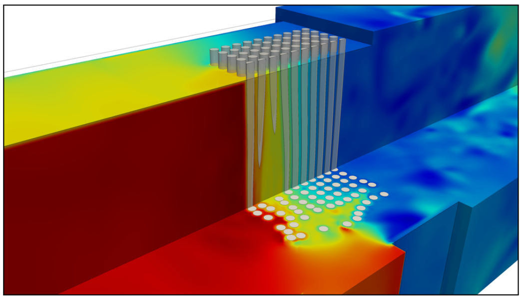

(o) Time = 12.5 ms

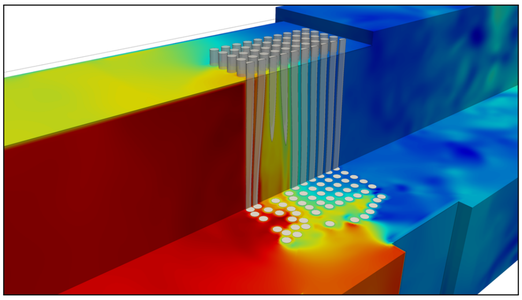

(p) Time = 13 ms ; increase global displacement of the rods compared to the 2.5 bars firing pressure case

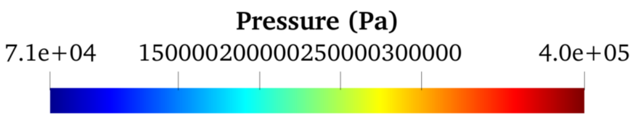

Figure 28: Firing pressure 5 bars, pressure field, zoom on rod bundle (continued)

Document property of CEA, issued in the framework of the agreement Tripartite Institute 2020 - F35158
Reproduction and transmission governed by the terms of the agreement

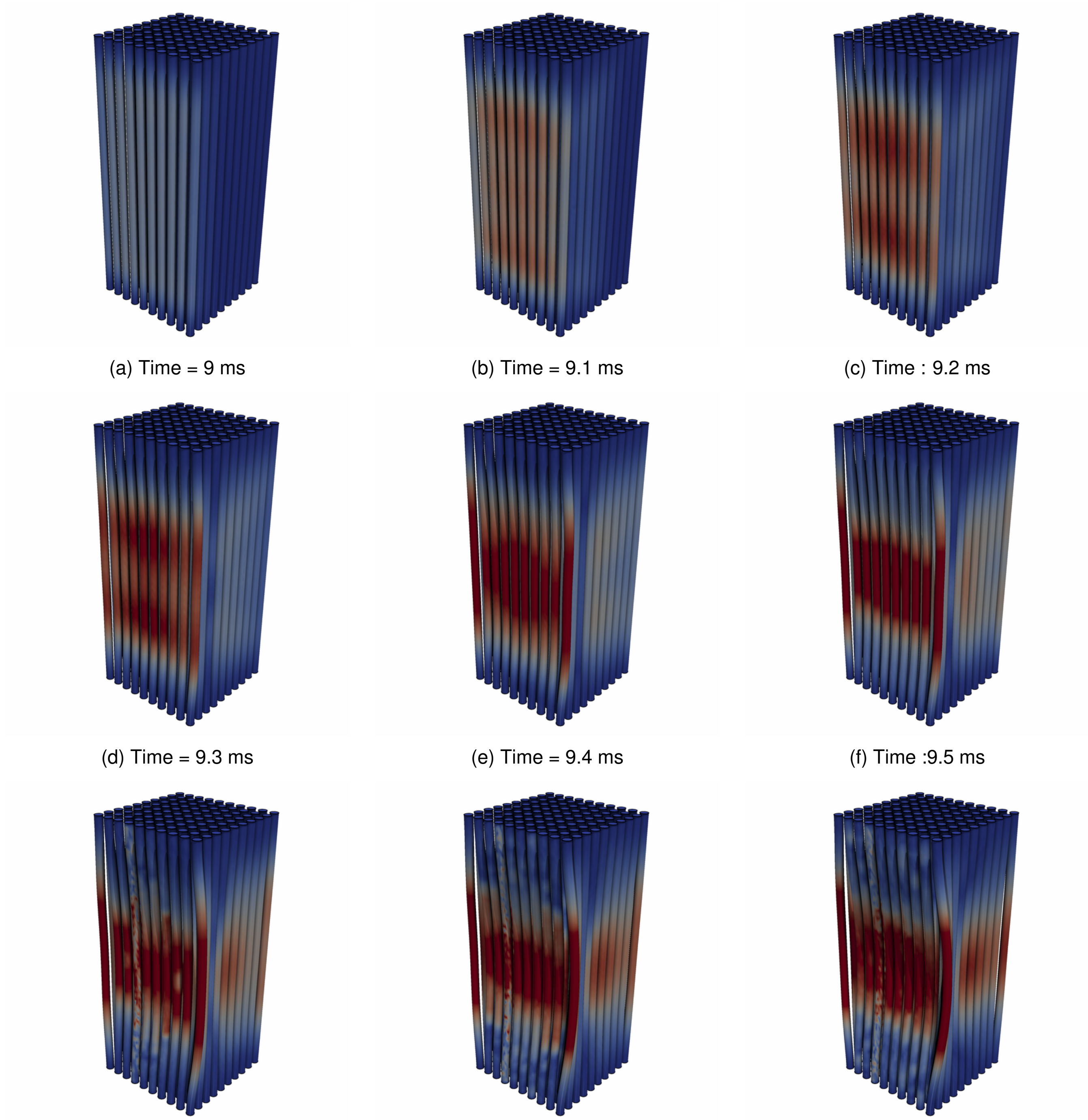

(a) Time = 9 ms

(b) Time = 9.1 ms

(c) Time : 9.2 ms

(d) Time = 9.3 ms

(e) Time = 9.4 ms

(f) Time :9.5 ms

(g) Time = 9.6 ms ; contact occurs between the first two rows of the bundle, sooner after the impact of the pressure wave than with the 2.5 bars firing pressure

(h) Time = 9.7 ms

(i) Time : 9.8 ms

Figure 29: Firing pressure 5 bars, bundle motion and rod velocities

Document property of CEA, issued in the framework of the agreement Tripartite Institute 2020 - F35158
Reproduction and transmission governed by the terms of the agreement

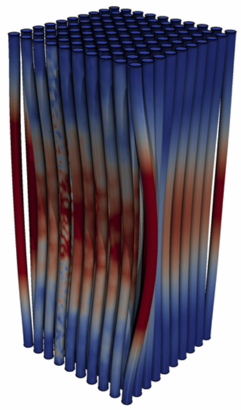

(j) Time = 9.9 ms

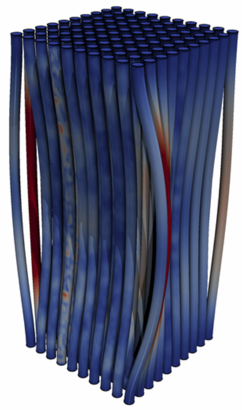

(k) Time = 10.5 ms

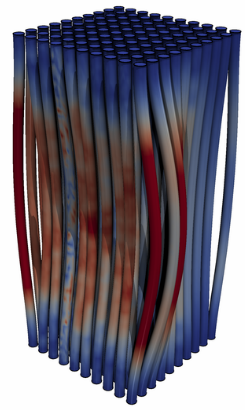

(l) Time : 11 ms

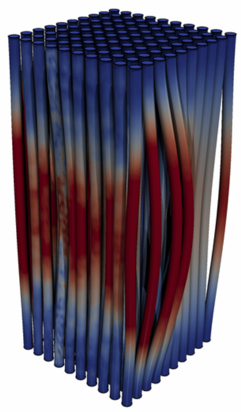

(m) Time = 11.5 ms

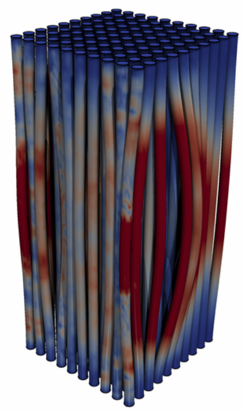

(n) Time = 12 ms

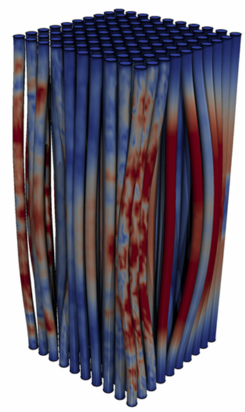

(o) Time : 12.5 ms

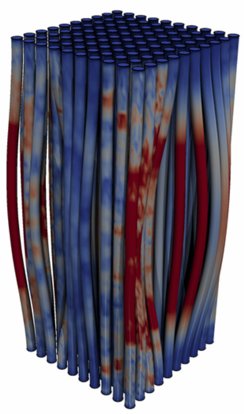

(p) Time = 13 m

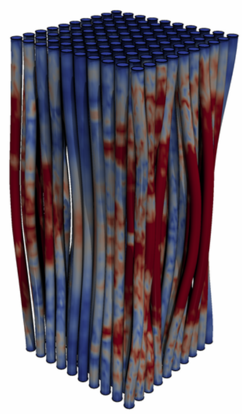

(q) Time = 16 ms ; the higher pressure wave results in enhanced multi-contact dynamics in the bundle

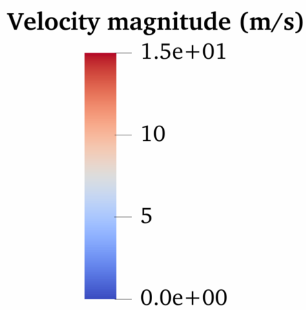

Figure 29: Firing pressure 5 bars, bundle motion and rod velocities (continued)

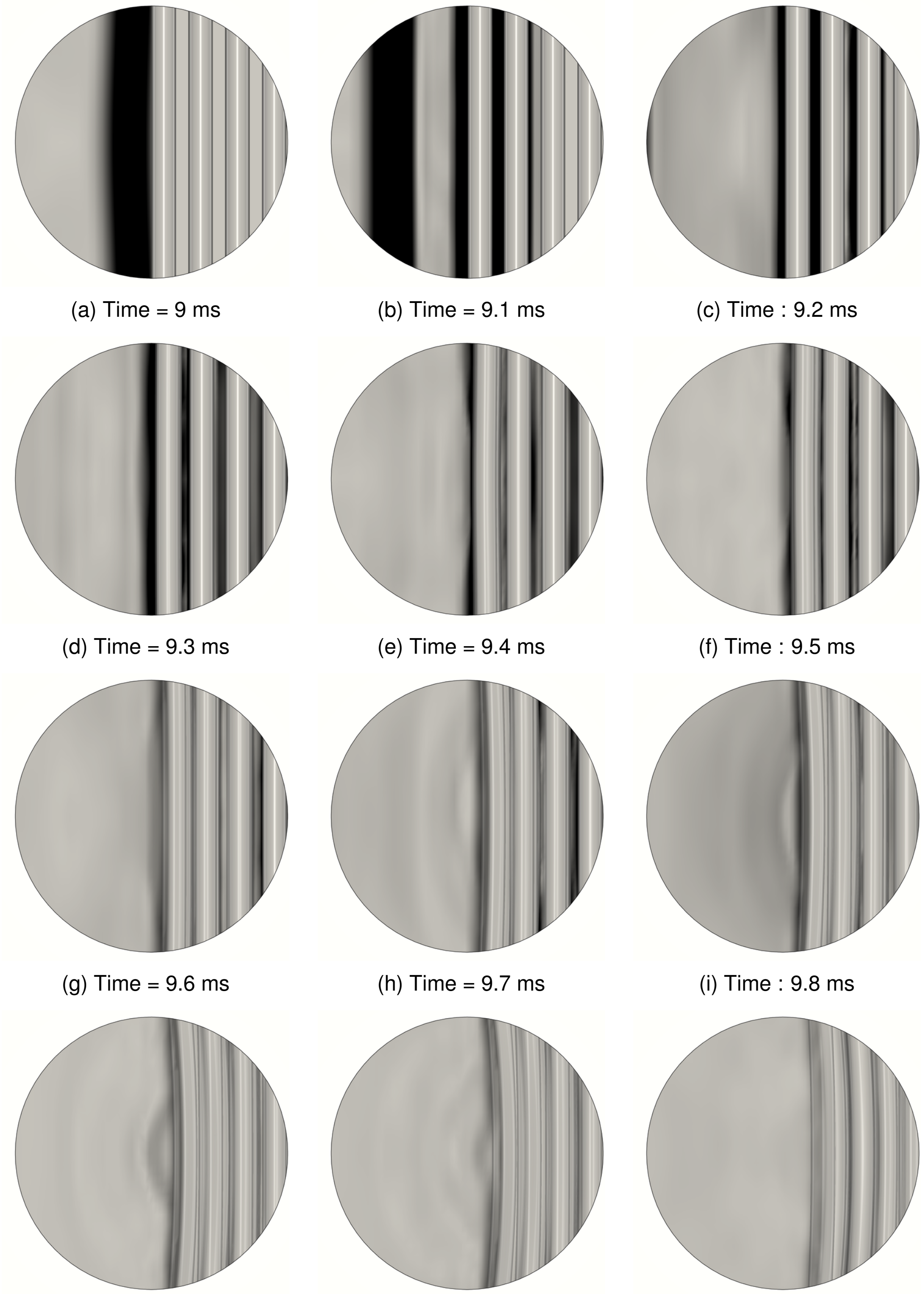

(a) Time = 9 ms (b) Time = 9.1 ms (c) Time : 9.2 ms

(d) Time = 9.3 ms (e) Time = 9.4 ms (f) Time : 9.5 ms

(g) Time = 9.6 ms (h) Time = 9.7 ms (i) Time : 9.8 ms

(j) Time = 9.9 ms (k) Time = 10.5 ms (l) Time : 11 ms

Figure 30: Firing pressure 5 bars, Schlieren representation for fluid density gradient and bundle motion through visualization window

Document property of CEA, issued in the framework of the agreement Tripartite Institute 2020 - F35158
Reproduction and transmission governed by the terms of the agreement

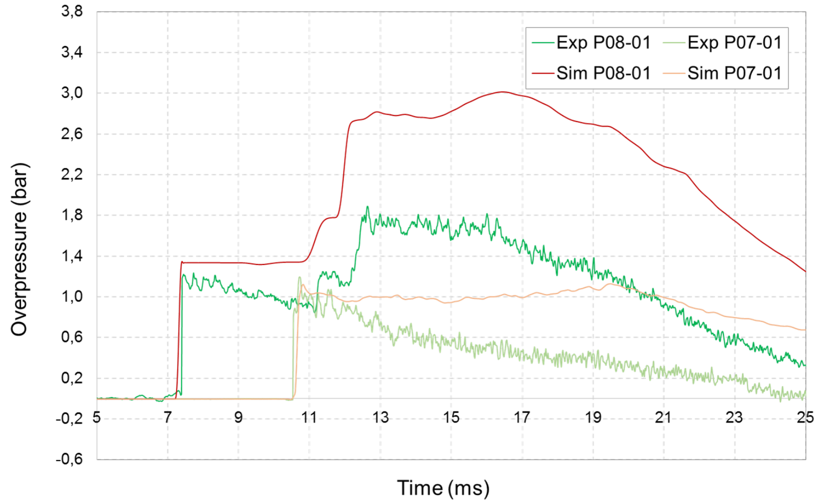

Figure 31: Firing pressure 5 bars, pressure evolution for Sensors P08-01 and P07-01

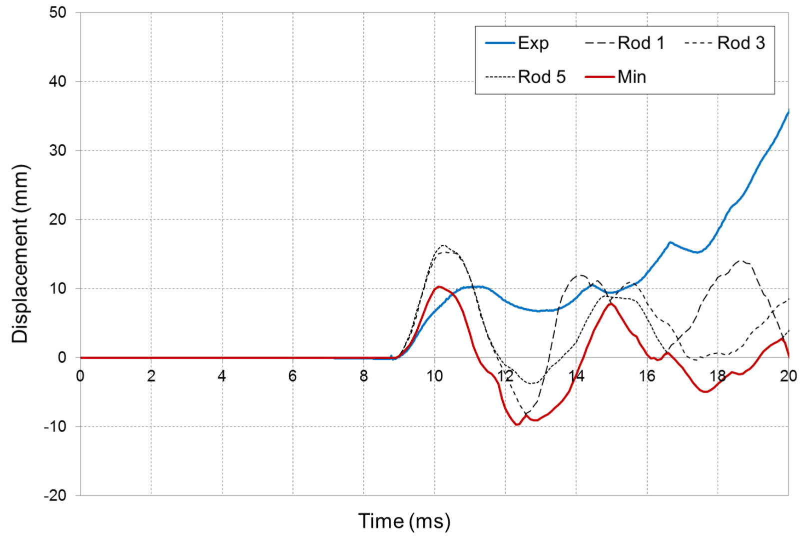

Figure 32: Firing pressure 2.5 bars, displacement of the first row of the bundle

Document property of CEA, issued in the framework of the agreement Tripartite Institute 2020 - F35158
Reproduction and transmission governed by the terms of the agreement

4.4 Analysis and comparison between experiment and simulation

The first results for experiment-simulation comparison are provided by Figure 25 for the 2.5 bars firing pressure case and Figure 31 for the 2.5 bars firing pressure case. Taking into account the differences in the pressure evolution after the initial jump related to the membrane dynamics not modelled in the simulation, the curves are in good agreement in both cases. The 2.5 bars firing pressure case is easier to interpret since it is closer to the theoretical shock tube solution, but both cases show similar features. In particular, the level and times of the pressure jumps measured at Sensor P08-01, related to the reflection of the incoming first on the entry of the supporting box and second on the rod bundle, are accurately reproduced. The transmitted waves are also correctly obtained, again for both time and level of the pressure jumps. The decaying slopes after the arrival of the rarefaction wave are also satisfactory, particularly in the 2.5 bars firing pressure case.

These results prove that the global fluid dynamics in the shock tube equipped with the proposed rod bundle specimen is correctly captured in the 3D model.

Regarding the bundle motion however and especially Figures 26 and 32, the results yield some reservations and it is not easy to discriminate which part can be attributed to the membrane dynamics. Comparing the experimental and numerical Schlieren outputs, it appears that the order of magnitude for the first rows of rods is rather correctly reproduced during the first oscillation just after the impact, namely from 8 mm of maximum deflection for the 2.5 bars firing pressure case, and 10 mm for the 5 bars case. The stiffer slope in the simulation after the first impact is consistent with the longer computed constant pressure state after the shock. The evolution of the bundle afterwards seems to differ in the experiment and in the simulation, and especially, the particular motion of the corner rods in the simulation does not seem to occur as clearly in the experiment. Some assumptions can be made to try and explain these discrepancies and should be confirmed or refuted by further work.

1. The longer duration of the constant pressure state after the shock in the simulation increases the impulse seen by the bundle, possibly leading to enhanced dynamics.

2. The reflection of the incoming wave on the windows in the lateral walls of the supporting can be higher in the simulation than in reality. The propagation of the wave on the other side of the wall, occurring in the experiment due to functional gaps needed to ensure that the box can be easily inserted in the tube, has been neglected in the simulation. This complementary flow could lower the level of the reflected wave, which seems to trigger the singular motion of the corner rods.

3. The fluid velocity inside and around the bundle must also be analyzed, since it significantly influences the pressure loading on the rods. To this extent, Figure 32 display the evolution of the velocity field in the mid-plane of the bundle in its vicinity. It can be seen that the flow between the rods is allowed with the proposed mesh size, but some artificial numerical reduction of the gap between the rods can be suspected. Anyway, it appears logical that the fluid flows preferentially in both bypass area around the bundle. Moreover, it appears that the opening of lateral gaps near the corner rods due the influence of the waves reflected on the windows allows an increasing flow in this area, amplifying the observed singular motion: this could be described as some kind of unstable behaviour of the bundle, difficult to predict or validate.

Document property of CEA, issued in the framework of the agreement Tripartite Institute 2020 - F35158
Reproduction and transmission governed by the terms of the agreement

From a test design point of view, this situation where the fluid flows preferentially around the rod bundle instead of through the bundle suggests some improvements in the perspective of future experiments. It provides little knowledge on the actual response of the bundle crossed by the wave as it should occur in the reactor configuration. It also yields more complicated wave propagation and interactions than initially expected, making the tests really challenging for the simulation. Anyway, the performed tests yet represent a very valuable base of knowledge for the validation of detailed 3D simulations, in the perspective of extensively using local numerical solutions to calibrate equivalent models for the bundle to get its response under various loading conditions. Some significant interpretation work also remains to be performed, with the necessary assessment of the sensitivity of the numerical solution to the actual pressure signals accounting for membrane dynamics, and more generally to a set of other uncertain parameters, among which the material properties for the PMMA (taken from the literature for the simulations among various grades of the material) and the representation of the boundary conditions at the ends of the rods).

Regarding specifically the expectations expressed in Section 1.3, the proposed tests cannot be considered as relevant to identify a transfer function directly associated to the bundle due to the statements above. They are however fully consistent with validation tasks for the detailed 3D simulations and the obtained results suggest that some work can be continued in this direction, even if the actual comparisons already provide some solid confidence in the 3D solver and the possibility to use it to produce numerical reference solutions. The potential improvements of the test setup have also been addressed above and mainly consist in designing a specimen surrounded by small bypass areas to emphasize the actual effects of the wave propagation through the bundle on its dynamics.

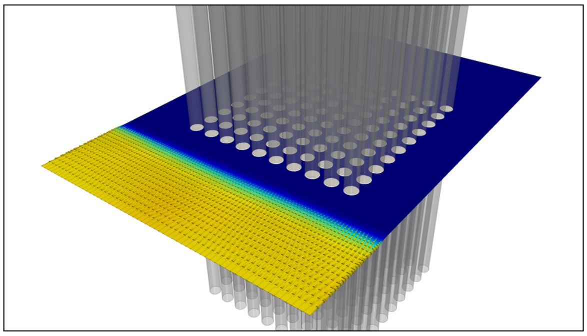

(a) Time = 9.9 ms

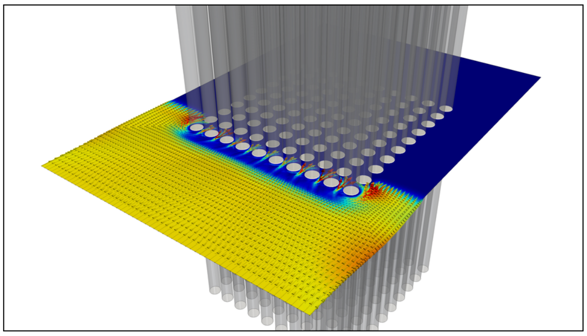

(b) Time = 10.0 ms ; most of the fluid is stopped by the bundle, with local flows through the first row of rods

Document property of CEA, issued in the framework of the agreement Tripartite Institute 2020 - F35158
Reproduction and transmission governed by the terms of the agreement

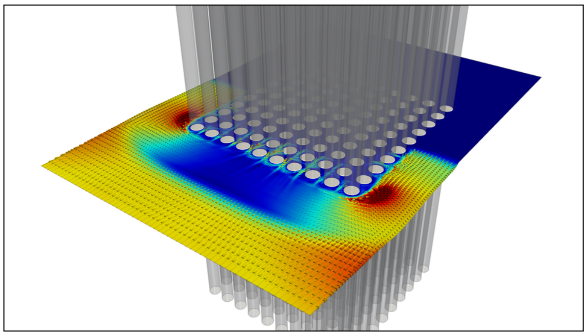

(c) Time =10.1 ms ; the fluid start to flow preferentially in the bypasses

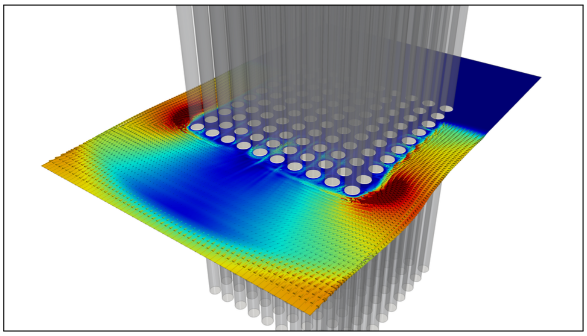

(d) Time = 10.2 ms ; lateral entries appear in the by-passes due to the reflected wave on the windows of the supporting walls

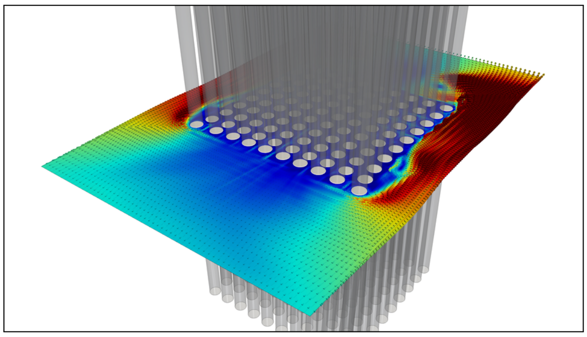

(e) Time = 10.7 ms

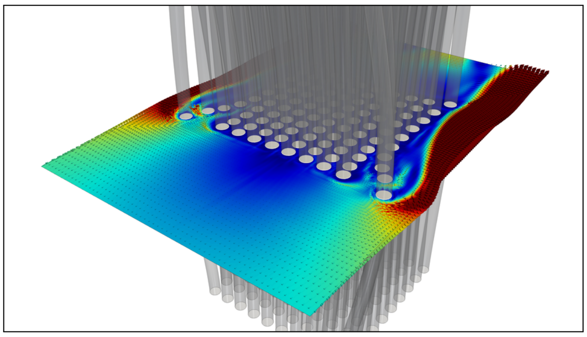

(f) Time = 11.9 ms ; the motion of the corner rods starts opening new channels for the fluid to flow, amplifying this motion

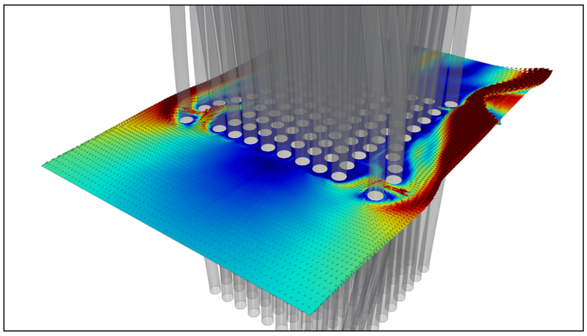

(g) Time = 12.0 ms

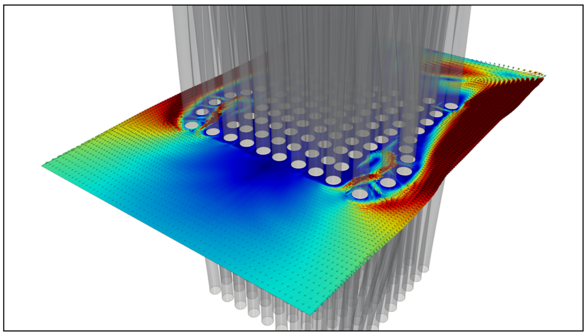

(h) Time = 12.1 ms

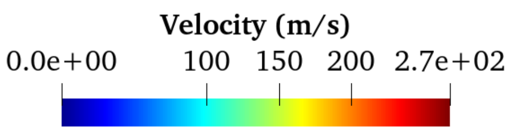

Figure 32: Firing pressure 2.5 bars, velocity field inside and around the rod bundle

5 Concluding remarks and prospects

A first series of tests has been successfully performed in the SIMLab Shock Tube facility to provide some insights regarding the dynamic response of a tube bundle submitted to a shock wave. The tests have provided very valuable results in terms of both pressure in the tube and resulting structural kinematics. The experiment has been extensively analyzed using numerical solutions to extend the measures and perform interesting steps towards the validated usage of 3D detailed Fluid-Structure simulations to produce reference solutions to build upper scale models of the bundle coupled dynamics, which is the main research topic of Samy Mokhtari's PhD motivating this work.

Some limitations have inevitably been encountered in this beginning research and the experimental results cannot be used directly to provide information about the transfer function associated to the bundle regarding the pressure signals upstream and downstream the specimen. This is mainly due to the large bypasses on both sides of the bundle, finally preventing the incoming wave to actually cross the bundle as it can be expected in the reference PWR configuration. Numerical simulations can also be further improved by taking into account the actual membrane opening dynamics for a better reproduction of the incoming pressure signals, as well as testing the sensitivity of the solution to modelling parameters in the vicinity of the bundle and its supporting box (*i.e.* the boundary conditions at the extremities of the rods and the potential fluid flow between the lateral walls of the box and those of the shock tube). This opens some interesting leads to continue and strengthen the collaboration between NTNU and CEA to keep producing knowledge on this subject of great value for nuclear safety.

Acknowledgements

This work has been carried out with scientific and financial support from CEA through the *Fuel Assembly* project from the *Reactors of 2nd and 3rd Generations* research program, NTNU and the Research Council of Norway through the Centre for Advanced Structural Analysis (CASA), Centre for Research-based Innovation (Project No. 237885). The financial support by the Norwegian Ministry of Justice and Public Security is also greatly appreciated.

References

[1] V. Faucher, F. Crouzet, F. Debaud. Mechanical consequences of LOCA in PWR: Full scale coupled 1D/3D simulations with fluid–structure interaction. Nuclear Engineering and Design **270**, p. 359-378 (2014).

[2] G. Ricciardi. Fluid-structure interaction modelling of a PWR fuel assembly subjected to axial flow. Journal of Fluids and Structures **62**, p. 156-171 (2016)

[3] S. Mokhtari, G. Ricciardi, V. Faucher, P. Argoul, L. Adelaïde. Multi-scale filtering of compressible wave propagation in complex geometry through a wavelet-based approach in the framework of Pressurized Water Reactors depressurization transient analysis. Fluids **5**(2), p. 64 (2020).

Document property of CEA, issued in the framework of the agreement Tripartite Institute 2020 - F35158
Reproduction and transmission governed by the terms of the agreement

[4] V. Aune, E. Fagerholt, M. Langseth, T. Børvik. A shock tube facility to generate blast loading on structures. International Journal of Protective Structures **7(3)**, p. 340-366 (2016).

[5] CEN. European Committee for Standardization. *NS-EN 13445: Unfired Pressure Vessels* (2014).

[6] F. Casadei, G. Valsamos, M. Larcher, V. Aune. Characterization of a shock tube facility by EUROPLEXUS. JRC Scientific and Technical Research Reports, JRC 112051. European Commission, Luxembourg (2018).

[7] V. Aune, G. Valsamos, F. Casadei, T. Børvik. Aspects of fluid-structure interaction on the dynamic response of blast-loaded metallic plates. Proceedings of the conference Light-Weight Armour for Defense and Security (LWAG), Roubaix, France, p. 102-111 (2019).

[8] EUROPLEXUS, A Computer Program for the Finite Element Simulation of Fluid-Structure. Users' Manual, available on website *http://www-epx.cea.fr*. Systems under Transient Dynamic Loading

Document property of CEA, issued in the framework of the agreement Tripartite Institute 2020 - F35158
Reproduction and transmission governed by the terms of the agreement